TeV Astronomy

J.A. Hinton[1] and W. Hofmann[2]

[1]School of Physics & Astronomy, University of Leeds, Leeds LS2 9JT, United Kingdom;
email: J.A.Hinton@leeds.ac.uk

[2]Department of Physics and Astronomy, Max Planck Institut für Kernphysik,
Heidelberg D-69029, Germany; email: werner.hofmann@mpi-hd.mpg.de

Key Words

gamma-ray astronomy, high-energy astrophysics

Abstract

Ground-based γ-ray astronomy, which provides access to the TeV energy
range, is a young and rapidly developing discipline. Recent discoveries in
this waveband have important consequences for a wide range of topics in
astrophysics and astroparticle physics. This article is an attempt to review
the experimental status of this field and to provide the basic formulae and
concepts required to begin the interpretation of TeV observations.

1. INTRODUCTION

Ground-based γ-ray astronomy effectively began in 1989, with the first robust detection of a TeV γ-ray source, the Crab Nebula, using the 10-m diameter air-Cherenkov telescope of the Whipple Observatory (Weekes et al. 1989). Nineteen years on, Cherenkov telescopes have been used to detect $\sim$80 very high energy (VHE; E > 100 GeV) sources, firmly establishing a new astronomical domain, and the first discoveries of sources using air-shower particle detectors have been made (Abdo et al. 2007a). The key advantage of ground-based instrumentation over satellite-based GeV instruments such as EGRET (Hartman et al. 1999) and the recently launched GLAST (now Fermi) large area telescope (LAT) (Thompson 2004) is collection area. The typical effective collection area of a single Cherenkov telescope is 10^5 m^2, almost five orders of magnitude larger than can realistically be achieved via direct detection in space. So far, the Imaging Atmospheric-Cherenkov Telescope (IACT) technique has proven to be the most powerful approach in this energy regime, with sensitivity of $\sim$1% of the flux of the Crab Nebula, angular resolution for single γ-rays of around 5′, energy resolution of $\approx$15%, and the ability to locate sources with precision down to 10″. The limitations of the IACT technique in comparison to air-shower particle detectors include a limited field of view ($\sim$5°) and a relatively poor duty cycle, with about 1000 h of useful observations obtainable per year.

The current status of VHE γ-ray astronomy is best summarized by **Figure 1**, showing the distribution of different types of VHE γ-ray source on the sky. In addition to a collection of extragalactic sources at high latitudes—identified as active galactic nuclei, a number of clearly Galactic sources line the Galactic equator. Their low latitudes imply kpc distances and most are extended with respect to the $\sim$5′ resolution of the instruments, implying emission region sizes of $\mathcal{O}(10$ pc$)$. These sources include shell-type supernova remnants, pulsar wind nebulae such as the Crab Nebula, binary systems, the Galactic Center, and a number of unidentified sources.

This review summarizes the basic emission mechanisms suspected to be active in these objects, provides a cookbook of useful formula for calculations in this field and gives an overview of the principal astrophysical results of TeV astronomy in the past few years. This article does not attempt to provide a complete list of VHE γ-ray sources and their properties—given the rapid progress in the field this task is better served by online databases such as *TeVCat*—but rather aims to illustrate key properties and mechanisms using selected objects. The reader is also referred to recent reviews covering related subjects, such as the review of high-energy astrophysics with ground-based detectors by Aharonian et al. (2008h) including a more detailed discussion of air-shower physics, the review of supernova remnants at high energy by Reynolds (2008), the discussion of whether acceleration in supernova remnants can account for galactic cosmic rays by Hillas (2005), the review of cosmic-ray propagation and interactions by Strong, Moskalenko & Ptuskin (2007), and the review of pulsar wind nebulae by Gaensler & Slane (2006).

2. GENERATION AND PROPAGATION OF VERY-HIGH ENERGY γ-RAYS

In this section some of the basic characteristics of acceleration and radiation processes relevant to VHE astronomy are summarized, providing simple expressions, approximations, and references to detailed work.

2.1. Particle Acceleration and Propagation

Except for possible production by top-down processes such as the decay of heavy particles, VHE γ-rays are produced only in the interactions of accelerated charged particles–nuclei or electrons
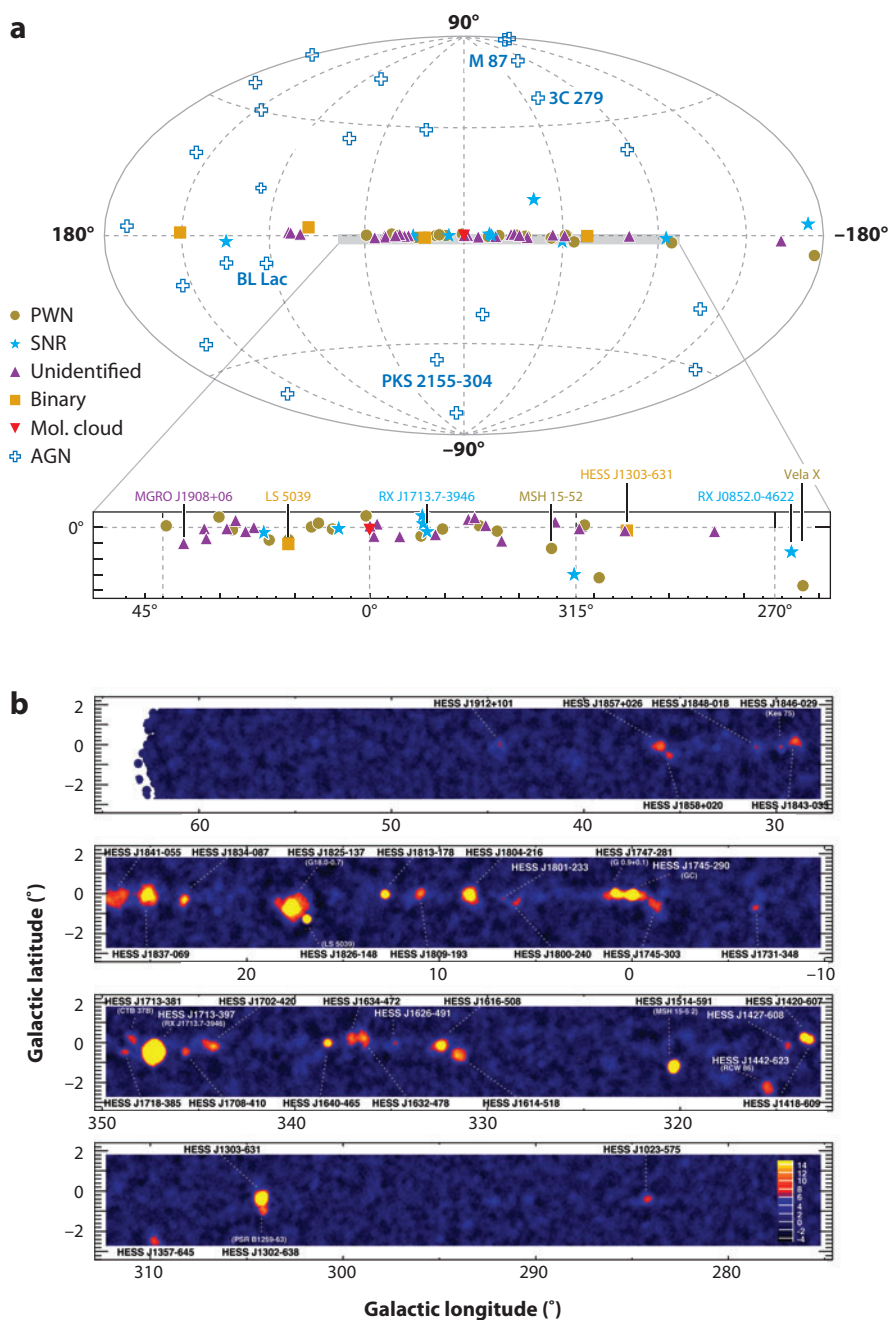
Figure 1

(*a*) The current catalog of VHE γ-ray sources plotted on the sky in Galactic coordinates. (*b*) The Milky Way viewed in VHE γ-rays: the HESS survey of the Galactic plane (reproduced from Hoppe et al. 2007).

(here and in the following, "electrons" stands for "electrons and positrons")—with ambient matter or radiation fields. The γ-ray production rate reflects the product of the densities of cosmic ray (CR) particles and "targets," tracking particles as they propagate away from the acceleration site owing to diffusion in magnetic fields or convection. γ-ray sources will therefore be extended objects, with sizes and shapes governed by particle flow speeds, distribution of targets, and possibly by the finite lifetime of particles due to interactions or radiative cooling. γ-ray sources that appear point-like, given the $\sim 5'$ resolution of current instruments, are either very distant (extragalactic), or associated with compact targets such as dense molecular clouds or stellar radiation fields.

Unless convective flows or bulk motion dominate, particle transport is governed by scattering off inhomogeneous ambient magnetic fields, resulting in diffusive propagation, $\langle r^2 \rangle = 2Dt$. The diffusion coefficient D is determined by the average strength B of the magnetic field and its degree of turbulence δB on length-scales comparable to the gyration radius R_g. The slowest possible diffusion in an isotropic medium is achieved in the Bohm limit $\eta = 1$, where the mean free path of particles is given by the gyration radius, resulting in $D \approx \eta R_g c / 3$ or, with $R_{g,pc} \approx 0.0011 E_{\mathrm{TeV}} / B_{\perp,\mu G}$, and particles of unit charge

$$\langle r_{\mathrm{pc}}^2 \rangle^{1/2} \approx 0.01 (\eta E_{\mathrm{TeV}} t_{\mathrm{yr}} / B_{\mu G})^{1/2}. \tag{1}$$

Typical interstellar fields are in $\mathcal{O}(3 \mu G)$. The coefficient η can be estimated as $\eta \approx (\delta B / B)^{-2}$ (Strong, Moskalenko & Ptuskin 2007). Bohm diffusion is very slow, compared, for example, with the speeds of young supernova shocks. Large-scale propagation in the Milky Way (e.g., Strong, Moskalenko & Ptuskin 2007) is governed by larger diffusion coefficients; in leaky box models one obtains $D \sim k 10^{28} E_{\mathrm{GeV}}^\alpha$ cm²/s, where k is a coefficient of order unity and $\alpha = 0.3$–0.6, or $\langle r_{\mathrm{pc}}^2 \rangle^{1/2} \sim (E_{\mathrm{TeV}}^\alpha t_{\mathrm{yr}})^{1/2}$, with the energy dependence reflecting the scale distribution of magnetic turbulence.

Diffusive shock acceleration is most likely the principle mechanism behind the production of high-energy particles, with supernova remnants (SNRs) believed to be one of the main sources of CRs. (For a recent overview of shock acceleration in SNRs, see Reynolds 2008). A supersonic flow, for example due to ejecta from a supernova explosion or a pulsar wind, terminates in a shock, balancing the pressure of the ambient medium. Best viewed in the rest frame of the shock, material is streaming into the shock from upstream at velocity u, is compressed by a compression factor r, and flows away from the shock with a speed reduced by the shock compression ratio. High-energy particles scatter off turbulent magnetic fields on both sides on the shock and may diffusively cross the shock many times. Each time they cross the shock and are isotropized by scattering in the medium on the other side, they gain an energy of order $\Delta E / E \approx u / c$. In each cycle, there is a finite probability for escape with the downstream flow, naturally creating a power-law spectrum of accelerated particles, $N(E) \sim E^{-\Gamma}$ with $\Gamma \approx (r+2)/(r-1)$, with $r = 4$ and $\Gamma \approx 2$ for shocks with high Mach number. Neglecting radiative cooling and adiabatic losses, the distribution of accelerated particles is uniform in the region downstream of the shock, where particles are swept away, and extends over a scale D/u into the upstream region. The acceleration rate $(1/E)(dE/dt) \approx u^2 / D$ is governed by the rate of shock crossings, determined by the diffusion coefficient. A small diffusion coefficient will keep particles near the shock and ensure rapid return across the shock front. The maximum energy is governed either by the finite lifetime of the shock, by synchrotron losses in case of accelerated electrons, or by the gyro-radius exceeding the shock size. Assuming Bohm diffusion, maximum proton energies achievable in supernova shocks of age $1000\, t_3$ years are of order

$$E_{\mathrm{max}} \sim u_8^2 t_3 B_{\mu G} \text{ TeV}, \tag{2}$$

where u_8 is the shock speed in units of $1000\,\mathrm{km\,s^{-1}}$ (e.g., Reynolds 2008); for electrons, synchrotron losses limit the peak energy to

$$E_{\mathrm{max}} \sim 100 u_8 B_{\mu G}^{-1/2}\,\mathrm{TeV}. \qquad (3)$$

(See Zirakashvili & Aharonian 2007).

In shock acceleration in SNRs, a significant fraction of kinetic energy of the flow can be transferred to high-energy particles. Once the energy density in particles is comparable to that in the shock, nonlinear effects start to play a role (see Caprioli et al. 2008, and references therein). The overall compression ratio r is increased beyond 4, but particles scattered upstream of the shock decelerate the inflowing material and generate a precursor, reducing the compression ratio at the main shock. Particles with gyro-radii that are small compared to the size of the precursor experience only the reduced compression ratio r, resulting in a steeper spectral index, whereas for the highest-energy particles $r > 4$. Hence, nonlinear shock acceleration produces concave spectra with $\Gamma \geq 2$ at low energy and Γ somewhat below 2 at high energy.

Both acceleration speed and maximum energy increase for small diffusion coefficients, i.e., from high magnetic fields and maximal turbulence of the field on all scales, resulting in $\eta \approx 1$. In this context, turbulent field amplification by streaming CRs has received increasing attention. Both resonant and nonresonant instabilities of the magnetic field are driven by CR currents (Lucek & Bell 2000; see Caprioli et al. 2008 for further references). In SNRs, magnetic fields can be estimated from the cooling length-scale of electrons produced at the shock front (see, for example, Berezhko, Ksenofontov & Völk 2003; Vink & Laming 2003), with results consistent with the predicted $B^2 \propto nu^3$ dependence, where n is the ambient density and u the shock velocity. Magnetic field amplification boosts the maximum energy of accelerated protons, but reduces the maximum electron energy due to increased losses.

2.2. Electronic Origin of γ-rays

Electrons produce high-energy radiation primarily via the inverse Compton (IC) process (Blumenthal & Gould 1970), by up-scattering ambient cosmic microwave background (CMB), infrared, optical, or, in special cases, X-ray, photons.

2.2.1. Energy-loss rates. in the Thomson limit, $b = 4E_e E_T/m^2 c^4 \ll 1$ or $b \approx 15 E_{e,\mathrm{TeV}} E_{T,\mathrm{eV}} \ll 1$, with E_e and E_T denoting electron and target photon energies, respectively, the energy loss rate is given by

$$\mathrm{d}E/\mathrm{d}t = (4/3)\sigma_T c \gamma^2 U_{\mathrm{rad}}. \qquad (4)$$

A black-body target radiation field can be approximated by setting E_T to $2.8\,kT$. At higher electron energies, around 300 TeV, 10 TeV, and 30 GeV for scattering off CMB, IR from dust and visible light, respectively, the Klein–Nishina (KN) regime begins and the energy loss rate is reduced, with a log E_e dependence in the deep KN regime. In general the cooling time, $\tau = E_e/(\mathrm{d}E_e/\mathrm{d}t)$, for IC scattering is given by

$$\tau_{\mathrm{yr}} = E_e/(\mathrm{d}E_e/\mathrm{d}t) \approx 3.1 \cdot 10^5 U_{\mathrm{rad,eV\,cm^{-3}}}^{-1} E_{e,\mathrm{TeV}}^{-1} f_{\mathrm{KN}}^{-1}, \qquad (5)$$

where the KN suppression factor f_{KN} can be parametrized as

$$f_{\mathrm{KN}} \approx (1 + b)^{-1.5} \approx (1 + 40 E_{e,\mathrm{TeV}} k T_{\mathrm{eV}})^{-1.5} \qquad (6)$$

for $b < 10^4$ (Moderski et al. 2005, and Erratum). The synchrotron cooling time is given by the very similar expression:

$$\tau_{\mathrm{yr}} = E_e/(\mathrm{d}E_e/\mathrm{d}t) \approx 1.3 \cdot 10^7 B_{\mu G}^{-2} E_{e,\mathrm{TeV}}^{-1}. \qquad (7)$$
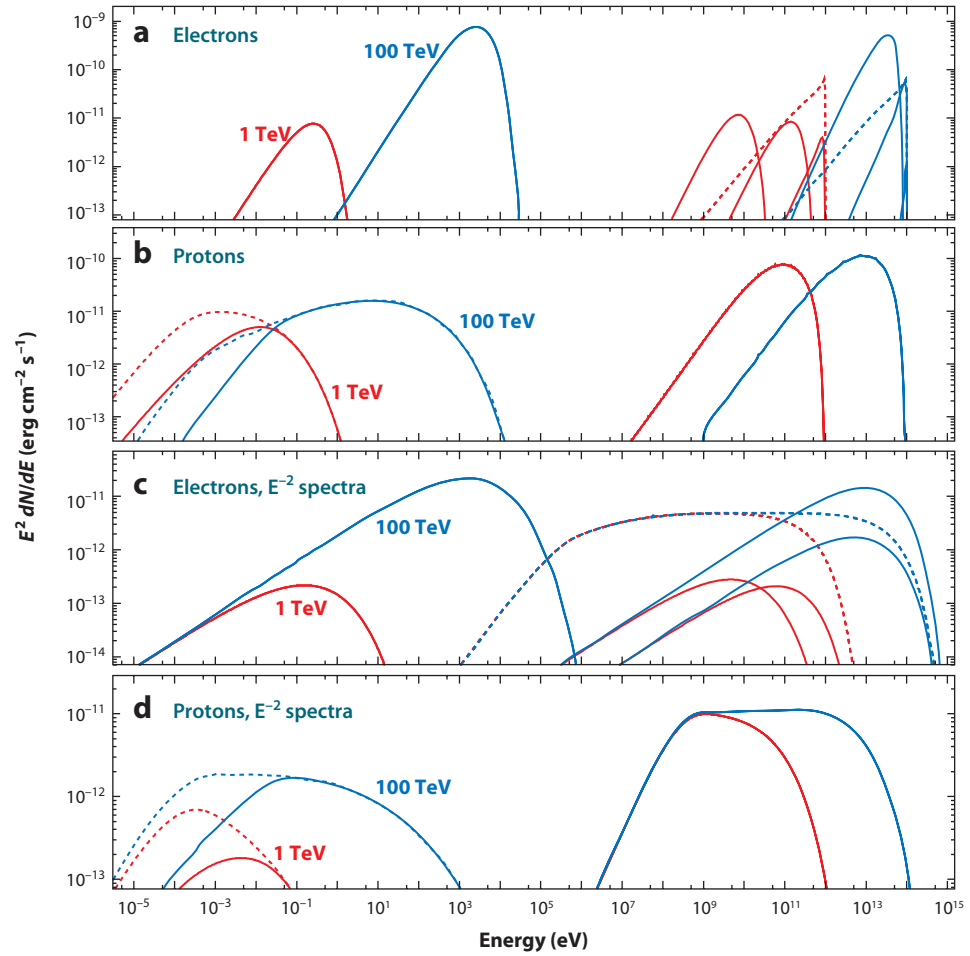
Figure 2

(*a*) SEDs for radiation of mono-energetic 1/100 TeV electrons (*red/blue curves*): Synchrotron and IC (*solid curves*) and Bremsstrahlung (*dashed curves*). Three IC curves are shown for each primary energy: (from low to high) on the CMB ($kT = 2.35 \times 10^{-4}$ eV, $b \approx 4 \times 10^{-3}/0.4$), on dust-emitted FIR ($kT = 0.02$ eV, $b \approx 0.3/30$), and on visible (star) light ($kT = 1.5$ eV, $b \approx 20/2000$). Note that for 100 TeV electrons scattering on optical photons the IC energy distribution is effectively a delta function at 100 TeV. The curve normalizations are appropriate for a total particle energy of 10^{48} erg at 1 kpc distance in a magnetic field of 3 μG, a matter density of 100 hydrogen atoms cm^{-3} and radiation fields of density 0.26 eV cm^{-3} (CMB and FIR) and 1 eV cm^{-3} (starlight). (*b*) SEDs for γ-rays and synchrotron radiation of secondary electrons from strong interactions of mono-energetic protons. The magnetic field is increased to 30 μG to illustrate the effects of cooling and steady injection over 10^4 years (*dashed curves* 10^5 years) is assumed. (*c*) and (*d*)—as for (*a*) and (*b*) but for cut-off power-law distributions of particles: $dN/dE \propto E^{-2} \exp{-E/E_c}$ with $E_c = 1$ TeV (*red*) and 100 TeV (*blue*).

2.2.2. Radiation spectra. scattering of mono-energetic electrons on a blackbody distribution of target photons of temperature T results in a broad spectral energy distribution (SED) of the resulting γ-rays (**Figure 2**). In the Thomson regime, energy losses are gradual and the γ-ray SED peaks at

$$E_{\gamma,\text{TeV}} \approx 33 E_{e,\text{TeV}}^2 k T_{\text{eV}}, \qquad (8)$$

resulting in

$$E_{e,\text{TeV}} \approx 11 E_{\gamma,\text{TeV}}^{1/2} \tag{9}$$

for scattering of CMB photons. In the KN regime, electrons tend to lose a large fraction of their energy in a single IC event and the corresponding SED peak energy is shifted to

$$E_{\gamma,\text{TeV}} \approx E_{e,\text{TeV}} \frac{2.1b}{(1 + (2.1b)^{0.8})^{1/0.8}}. \tag{10}$$

The equivalent expression for the typical energy of synchrotron photons is

$$E_{s,\text{eV}} = 0.087 E_{e,\text{TeV}}^2 B_{\mu\text{G}}. \tag{11}$$

Although the energy-loss rate of electrons depends (in the Thompson regime) only on the energy density in target radiation fields, the spectrum of γ-rays is strongly influenced by the spectral distribution of target photons (**Figure 2**). Since in the Thomson limit the γ-ray energy scales with the square of the electron energy, the IC γ-ray spectrum is harder than the spectrum of parent electrons: Assuming isotropic distributions of electrons and target photons, a power-law distribution of electrons $N_e(E) \sim E_e^{-\Gamma_e}$ will generate IC (and synchrotron) spectra of index $\Gamma_\gamma = (\Gamma_e + 1)/2$, $\Phi_\gamma \propto E_\gamma^{-(\Gamma_e+1)/2}$. Deep in the KN regime, γ-ray spectra steepen by $\Delta\Gamma_\gamma \approx (\Gamma_e + 1)/2$, $\Phi_\gamma \sim E_\gamma^{-(\Gamma_e+1)}$, up to log E_γ terms (Blumenthal & Gould 1970). Therefore, even for a pure power-law distribution of electrons, γ-ray spectra exhibit a break corresponding to the transition to the KN regime.

IC γ-rays of energy E_γ (in the Thomson regime) and synchrotron photons of energy E_{sync} probe the identical electron population provided that $E_{\gamma,\text{TeV}} = 380 E_{\text{sync,eV}}(kT_{\text{eV}}/B_{\mu\text{G}})$. For example, 11 TeV electrons produce both 1 TeV IC photons (on the CMB) and 1 keV synchrotron photons, if $B = 100$ μG. In this case, the ratio of energy flux in the synchrotron and IC bands is just $U_{\text{mag}}/U_{\text{rad}}$, allowing the magnetic field strength in the source region to be determined. For the smaller (several μG) fields found typically in the ISM, X-ray synchrotron emission traces electrons of considerably higher energies than the TeV IC γ-rays and a model for the shape of the electron spectrum is required to deduce the magnetic field.

Which target photon fields are most relevant for γ-ray production depends on the electron spectrum and on the γ-ray energy considered. The relative yields of CMB target photons, IR target photons, and visible target photons vary depending on the location of sources, e.g., with Galacto-centric radius, and with the proximity of strong radiation sources. At the location of the sun, typical radiation energy densities are 0.3 eV cm^{-3} for IR from dust, and 0.3 eV cm^{-3} for visible light (see Porter, Moskalenko & Strong 2006) (cf 0.26 eV cm^{-3} for the CMB). For electron spectra without a cutoff, CMB photons will often dominate at sufficiently high energies, as the contributions of IR and visible photons are suppressed in the KN regime. In this case, γ-rays directly map the distribution of VHE electrons. For electron spectra with a cutoff, the situation can, however, be reversed, with the efficient transfer of energy from an electron to a γ-ray overcompensating for the drop in scattering cross-section.

Electrons passing through a medium containing atoms or plasma will also create γ-rays by Bremsstrahlung (Blumenthal & Gould 1970). The loss timescale is energy-independent, with loss rates and spectra depending on the state of the medium (mainly the shielding length for ions). For neutral hydrogen atoms of density n per cm^3, $\tau = E_e/(dE_e/dt) \approx 3.9 \cdot 10^7 n^{-1}$ years. IC scattering on the CMB dominates in the 1 TeV emission of electrons in (neutral) media as long as $n < 240$ cm^{-3}. Bremsstrahlung γ-ray spectra produced by a power-law distribution of electrons are also power laws, with $\Gamma_\gamma = \Gamma_e$.

2.3. Modeling Radiation Spectra from Electron Populations

Energy losses by synchrotron radiation or IC will modify electron spectra compared to the index at injection Γ_i above energies where the energy loss time (Equation 7) becomes comparable to the age T of the electron source. If synchrotron losses or IC losses in the Thomson regime dominate, $(dE/dt)_{\text{sync+IC}} = -\kappa E^2$, the electron energy distribution will be cut off (for burst injection in a source of age T_s) at $E = 1/(\kappa T_s)$, the energy where the radiative lifetime $(1/E)(dE/dt)$ equals the age T_s, or will exhibit a spectral break at the same energy, with index Γ_e increasing by 1 (in case of continuous injection over time T_s) (Kardashev 1962). This will cause a cutoff or break with index change $\Delta\Gamma_\gamma = 1/2$ in IC and synchrotron spectra at the corresponding energies (Equations 8, 11). The situation is more complicated if IC losses dominate over synchrotron losses, as might be the case near strong radiation sources, as discussed by Moderski et al. (2005). Entering the KN regime, electron energy losses are reduced, resulting in a harder "cooled" spectrum $\Gamma_e \approx \Gamma_i + 1 + \Delta\Gamma$ with $\Delta\Gamma \approx -1\ldots-1.5$, and $\Gamma_\gamma \approx \Gamma_i$. With IC losses scaling slower than E_e^2, synchrotron losses will, however, always dominate above a certain energy, causing Γ_γ to change to $\approx\Gamma_i + 2$. **Figure 3** shows the effects of both IC and synchrotron dominated cooling on the SED from an injected power law of relativistic electrons.
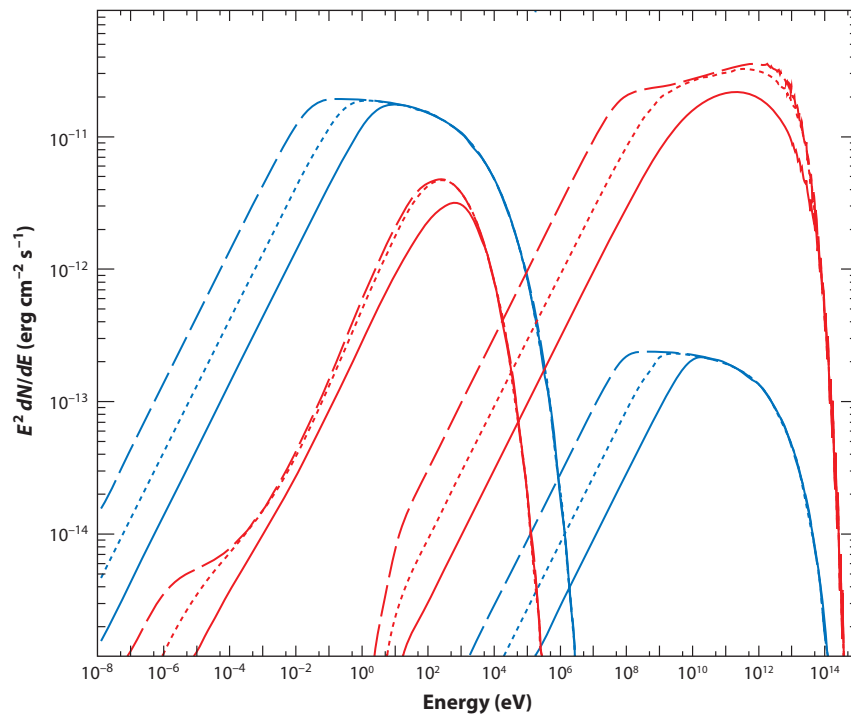

Figure 3

SEDs for continuous injection and cooling of a population of electrons with an E^{-2} injection spectrum and an exponential cut-off at 100 TeV. Solid, short-dashed and long-dashed curves show injection timescales of 10^4 years, 3×10^4 years, and 10^5 years, respectively. The blue curves show synchrotron and IC emission in the case of synchrotron-dominated cooling, with $B = 30$ μG and the CMBR as target for IC. The red curves illustrate the effects of IC-dominated cooling with a lower magnetic field ($B = 3$ μG) and a higher-energy radiation field (black-body photons with $kT = 1.5$ eV, with density 1000 eV cm^{-3}) where KN effects become important.

The above discussion assumes particle injection with a power-law spectrum, followed by radiative losses. If acceleration timescales and loss timescales are comparable, acceleration and losses cannot be factored and complex spectral patterns can arise, as discussed, for example, by Zirakashvili & Aharonian (2007).

In modeling radiation spectra of astrophysical sources, several approaches are followed:

- One can determine the spectrum (and composition) of particles that, interacting with suitable target fields and radiation fields, gives rise to the observed wide-band SED (e.g., Aharonian et al. 2005d).
- One can determine the energy spectrum of injected particles that, after accounting for the modification of the spectrum over time due to radiation losses and interactions etc., creates the observed SED (e.g., Hinton & Aharonian 2007; **Figure 3**).
- One can model the full dynamics of the source, including particle acceleration mechanisms, losses, and interactions (e.g., Berezhko & Völk 2006).

The first approach is self-consistent but has the potential problem that, because of the many degrees of freedom in the choice of spectral parametrisation and targets, it may be difficult to arrive at a unique solution. Frequently, spectral parametrization assumes a broken power law, with the fit sometimes resulting in a large increase in spectral index at the break (see, for example, Aharonian et al. 2005d). It is nontrivial to see which mechanisms would produce such spectra; at synchrotron cooling breaks in electron spectra, the index increases only by one.

The second intermediate approach attempts to cure this deficit by including (some of) the mechanisms that cause spectral breaks and cutoffs. However, simplifying assumptions are often made concerning the history of particle injection. In sources where particles are confined within an expanding envelope, such as SNRs or pulsar wind nebulae, adiabatic losses usually need to be taken into account, but frequently are not. Cooling during acceleration may modify injection spectra compared to the often assumed power law. This approach usually gives reliable answers only if cooling times are short compared to the evolution/expansion timescales of the system, but long compared to acceleration timescales.

The third approach is "best" in that it attempts to account for all relevant effects, but is most demanding and has the disadvantage that solutions are usually numerical and that it is nontrivial to understand the systems in terms of a clear one-to-one connexion between input assumptions and predicted radiation SED.

2.4. Hadronic Origin of γ-rays

An alternative source of VHE γ-rays are interactions of high-energy protons and nuclei with interstellar material. Through this mechanism, γ-ray emission traces CR acceleration sites and CR propagation, as demonstrated in the GeV energy range by the study of diffuse γ-ray emission from the Milky Way (Hunter et al. 1997). The interaction cross section of VHE protons on hydrogen nuclei of density n per cm^3 is only weakly energy-dependent, $\sigma_{pp,\text{inel}} \approx 35$ mb, resulting in a lifetime of $\tau \approx 3 \cdot 10^7 n^{-1}$ yr at multi-TeV energies. The number of secondary particles produced per interaction increases with energy. Typically, half of the energy E_p of the primary is carried away by a leading nucleon, and the other half is split between charged and neutral pions and a small fraction of heavier hadrons. This implies that about 1/6 of the primary energy is carried by a number of γ-rays produced in π^0 decays. To a good approximation, and for $E_\gamma \gg m_\pi$, the distribution in energy of γ-rays produced per interaction is scale invariant, $dn_\gamma/dE_\gamma(E_\gamma, E_p) = D_\gamma(x = E_\gamma/E_p)$. Parameterizations for the fragmentation function D are given, for example, by Kelner, Aharonian & Bugayov (2006). **Figure 2** illustrates the SED of γ-rays produced by mono-energetic protons.

The SED of secondary γ-rays peaks at about 1/10 of the energy of the primary. For a power-law proton distribution $dn_p/dE_p = k_p E_p^{-\Gamma}$ the γ-ray distribution is again a power law with the same index:

$$\frac{dn_\gamma}{dE_\gamma dt} = cn\sigma_{pp,inel}\int_{E_\gamma}\frac{dn_p}{dE_p}D\left(\frac{E_\gamma}{E_p}\right)\frac{dE_p}{E_p} = cn\sigma_{pp,inel}\,k_p E_\gamma^{\Gamma}\int_0^1 D(x)x^{\Gamma-1}\,dx. \qquad (12)$$

It is convenient to write this as

$$\frac{dn_\gamma}{dE_\gamma dt} = cn\sigma_{pp,inel}\,\kappa k_p\left(\frac{E_\gamma}{f}\right)^{-\Gamma}, \qquad (13)$$

since for $f \approx 0.15$ the coefficient $\kappa \approx 6$ is approximately constant for Γ between 2 and 4. This property should not be misinterpreted in the sense of a delta-function approximation, namely that in general the γ-ray spectrum at energy E_γ traces the proton spectrum at energy E_p/f. In particular, Kelner, Aharonian & Bugayov (2006) show that an exponential cut-off in the proton spectrum, $\exp(-E_p/E_{cut})$, is transformed into a more gradual cut-off, $\exp(-(16E_\gamma/E_{cut})^{1/2})$ in the γ-ray spectrum. Obviously, given the width of the γ-ray SED illustrated in **Figure 2**, any feature in the proton spectrum will reappear smoothed in the γ-ray spectrum.

One application is the estimation of the γ-ray flux from molecular clouds illuminated by CRs, possibly from a nearby accelerator. For a cloud of mass M and distance d illuminated by a proton flux $\Phi(E) = k_p E_p^{-\Gamma}$ (per area, solid angle, and energy), one obtains a γ-ray flux

$$\Phi_\gamma(E) = \frac{\sigma_{pp,inel}}{d^2}\frac{M}{m_H}\kappa k_p\left(\frac{E_\gamma}{f}\right)^{-\Gamma} \qquad (14)$$

with the hydrogen mass m_H. With a small correction for heavier nuclei and assuming a CR proton flux as measured on Earth, this translates, for example, into a flux

$$\Phi_\gamma(>1\,\mathrm{TeV}) \approx 1.6\cdot10^{-12}M_6/d_{\mathrm{kpc}}^2\,\mathrm{cm}^{-2}\,\mathrm{s}^{-1}, \qquad (15)$$

where M_6 is the cloud mass in units of 10^6 solar masses (see, for example, Aharonian 1991). These estimates assume that the CRs permeate the cloud; the increased magnetic fields inside dense clouds may, however, influence the diffusion coefficient and hence the spectrum and flux of CRs. In the case of clouds illuminated by nearby CR accelerators that were active for a relatively short time, energy-dependent diffusion will modify the spectrum at the cloud as compared to the spectrum generated at the accelerator; high-energy particles reach the cloud first, resulting in a harder γ-ray spectrum at the cloud (see Gabici, Aharonian & Blasi 2007, and references therein).

Dense environments will also result in production of Bremsstrahlung γ-rays by electrons; assuming that electron and proton spectra are identical and that the ratio of electrons to protons is k_{ep}, one obtains a flux ratio $\Phi_{\gamma,\mathrm{brems}}/\Phi_{\gamma,\mathrm{hadr}} \approx 3.3\,k_{ep}$ at 1 TeV, with only weak dependence on photon energy due to the changing σ_{pp} (in the region far from cut-offs).

2.5. Absorption During Propagation and Opacity of Sources

The mean free path of VHE γ-rays in hydrogen gas is governed by the electron-positron pair production cross section and has a value of 80 g cm^{-2} or equivalently 5×10^{25} hydrogen atoms cm^{-2}; for all practical purposes, the universe is transparent to this process. The more relevant process is the absorption by pair production on ambient (CMB, IR, visible or X-ray) photons of energy E_T. The process acts above the threshold $E_\gamma E_T = m^2c^4$ or $E_{\gamma,\mathrm{TeV}} = 0.26/E_{T,\mathrm{eV}}$ and the absorption cross section for an isotropic photon field $\sigma_{\gamma\gamma}$ (see, for example, Aharonian, Khangulyan & Costamante 2008) peaks close to threshold at $E_{\gamma,\mathrm{TeV}} = 0.9/E_{T,\mathrm{eV}}$. **Figure 4** illustrates absorption by different (blackbody and power-law) photon spectra.
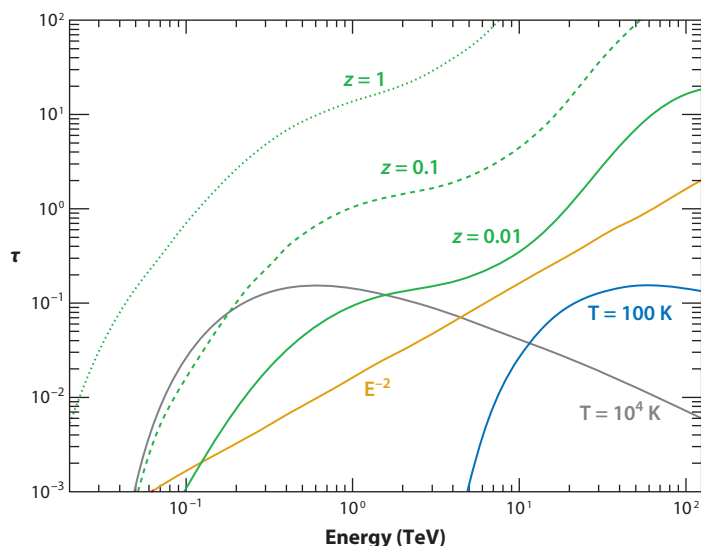
Figure 4

Optical depth (τ) of γ-rays as a function of energy, for FIR ($kT = 0.008$ eV) and visible ($kT = 0.8$ eV) target photon fields, of column density $3 \cdot 10^{22}$ eV cm^{-2} for FIR (1 eV cm^{-3} over 10 kpc) and $3 \cdot 10^{24}$ eV cm^{-2} for visible (1 eV cm^{-3} over 1 Mpc). The effect of absorption on a nonthermal photon distribution (with $dN/dE \propto E^{-2}$) is shown for comparison. Note that the absorption is constant for an E^{-1} photon field. The green curves show the optical depth for pair production on the EBL for redshifts of 0.01, 0.1 and 1 for the model of Franceschini, Rodighiero & Vaccari (2008).

Two situations where absorption is important are (*a*) the observation of extragalactic sources and (*b*) TeV emission near intense sources of radiation. **Figure 4** also shows the optical depth for VHE γ-rays interacting with intergalactic radiation fields taking into account cosmological evolution of the background fields; the range of γ-rays is about $z = 0.03$, $\sim$0.1, $\sim$1 for $E_\gamma = 10$, $\sim$1, $\sim$0.1 TeV. At PeV energies, the range is reduced to galactic distance scales. At energies up to tens of TeV, on the other hand, absorption of galactic sources is almost negligible (**Figure 4**), even for sources near the Galactic Center with its increased radiation fields (Moskalenko, Porter & Strong 2006).

Absorption is relevant for γ-rays produced in radiation-intensive environments, for example, in systems of compact objects in close orbit around massive stars. Radiation produced, for example, in a massive X-ray binary at 0.1 AU from the massive star traverses $\mathcal{O}(10^{27})$ eV cm^{-2}, resulting in a large optical depth at TeV energies if the γ-ray source is behind the star, allowing head-on collisions between γ-rays and stellar photons. Because of the peaked absorption cross section, narrow (black-body) background photon spectra cause selective absorption in part of the VHE energy range and lead to significantly modified spectra (see **Figure 4** and Aharonian, Khangulyan & Costamante 2008). In such dense absorbers, the electrons produced may undergo IC scattering, creating a pair cascade that proceeds until γ-ray energies are low enough that the medium becomes transparent. The absorption dip in the γ-ray spectrum is then accompanied by a corresponding enhancement at lower energies (for example, see Protheroe & Stanev 1993). Absorption within the source is also a key factor for γ-ray emission from compact regions (knots, blobs) within AGN jets, due to the high radiation density in these regions (see Section 4.6).
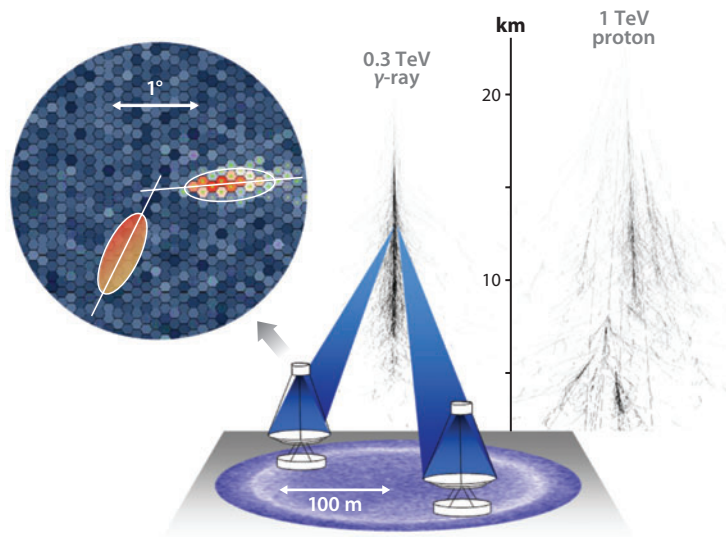
Figure 5

A sketch of the imaging atmospheric Cherenkov technique showing the formation of an electromagnetic cascade for a 300 GeV photon primary, the production of Cherenkov light, and the formation of an image in the camera of a Cherenkov telescope. Cherenkov light production for a proton initiated cascade is shown for comparison. Shower images produced by Konrad Bernlöhr.

3. INSTRUMENTS FOR TeV ASTRONOMY AND THEIR CHARACTERISTICS

Given the very low fluxes of γ-rays in the VHE regime–$\mathcal{O}(10^{-11})$ photons per cm^2-second (a few photons per m^2-year) above 1 TeV for strong sources, direct detection by space-based instruments is excluded. Ground-based instruments detect secondary products resulting from the development of γ-ray initiated air-showers: either particles reaching the ground or Cherenkov light emitted by shower particles in the atmosphere. In contrast to the well-collimated electromagnetic air-showers induced by γ-rays (or electrons), air-showers initiated by CR nucleons typically feature a number of electromagnetic subshowers induced by π^0 decays and contain muons from charged pion decays (see **Figure 5**). Rejection of the background of showers initiated by charged CRs is a key performance criterion for γ-ray detection systems, and is usually achieved on the basis of shower shape or muon content. A more detailed discussion of air-shower characteristics and the detection systems used can be found, for example, in Aharonian et al. (2008h).

3.1. Instrument Characteristics

For ground-based instruments detecting γ-rays via their shower development in the atmosphere, effective detection areas, $A(E)$, (defined such that the differential detection rate $R_\gamma(E) = \Phi_\gamma(E)A(E)$), have a subthreshold region where they exhibit a steep rise with energy, and a high-energy region where $A(E)$ varies only weakly with energy. In the subthreshold region, the detector triggers only because of favorable fluctuations in the development of an air-shower. In the high-energy region, every air-shower within a certain fiducial region is recorded. The "energy threshold" of a detection system is usually quoted as the energy at which the peak detection rate $R(E)$ occurs for typical power-law γ-ray spectra. The threshold thus determined obviously

depends on the assumed spectral index, but is always located in the transition region between the steeply rising part and the nearly constant region of $A(E)$. Individual events may be detected at energies well below this nominal threshold.

Two criteria govern detectability of a source during an exposure time T: (a) A minimum number n_0 (usually 5..10) of γ-rays must be detected, $TR_\gamma > n_0$, and (b) the γ-ray signal must be be significant above fluctuations in the background, approximately $(TR_\gamma)/(T\eta_{CR}R_{CR}\Omega)^{1/2} > \sigma_0$. Here, R_{CR} is the detection rate of background CRs per solid angle, η_{CR} the efficiency for CRs passing analysis cuts relative to the corresponding efficiency for γ-rays, and Ω the solid angle over which the signal from a source has to be integrated, given either by the point spread function (PSF) of the instrument or the source size. For point sources and a Gaussian PSF, $\Omega \approx \pi\theta_{68}^2$, where θ_{68} is the 68% containment radius of the PSF. Current instruments typically operate in the background-dominated regime, implying that minimal detectable fluxes scale as $T^{-1/2}\eta_{CR}^{1/2}\theta_{68}$. For sources that are large compared to the PSF, $\Omega \approx \pi\theta_s^2$, and sensitivity degrades linearly with source radius θ_s.

3.2. Cherenkov Imaging of Air-Showers

In the past decade, Imaging Atmospheric Cherenkov Telescopes (IACTs) have emerged as the most powerful instrument for pointed observations of VHE γ-ray sources. IACTs use focusing mirrors to image the Cherenkov light emitted by shower particles onto a pixelated photon detection system (see **Figure 6**); a summary of the characteristics of current and selected previous instruments is given in **Table 1**.

At the maximum of the shower development, around 10 km a.s.l. for TeV energies, the Cherenkov threshold for electrons is around 40 MeV and the Cherenkov angle is 0.7° or less. Light emitted at the Cherenkov angle reaches the ground within a circle of 100 to 150 m depending on the height above sea level of the detection system. Multiple-scattering angles of shower particles near the Cherenkov threshold are comparable to the Cherenkov angle, resulting in a more or less uniformly filled light pool, with typically 10 detected Cherenkov photons per TeV shower energy and m^2 mirror area for photomultiplier sensors. With increasing energy, the central density in the light pool is enhanced due to deeper penetration of showers. Triggering and image reconstruction usually requires 50 to 100 detected photons and sets the scale for the dish size. The pixel size of the detection system should be matched to the size of features in air-shower images; simulation studies show saturation of performance for pixels much below 0.1° diameter—close to the typical rms width of a γ-ray image at TeV energies. The asymptotic collection area for IACTs is determined by the maximum impact distance for which shower images still fall within a camera and hence by the camera field of view (FOV). At 2000 m a.s.l. the impact distance limitation is approximatey 100 m per degree of the opening angle of the camera field of view (for showers close to Zenith **Cap, as below**).

Most modern instruments use multiple telescopes (a) to image the air-shower from different viewing angles for improved reconstruction of γ-ray direction and rejection of CR background and (b) to apply a coincidence requirement rejecting single-telescope triggers caused by CR muons with impact points close to a telescope mirror, or by night-sky background. Telescope spacing needs to be large enough to provide a sufficient baseline for stereoscopic measurements, but small enough that multiple telescopes fit within the Cherenkov light pool; the exact spacing tends to be uncritical within a range of ~70 m to 150 m. Depending on selection cuts, telescope systems such as H.E.S.S. (**Table 1**) provide an angular resolution for single γ-rays of 3′ to 6′, a γ-ray energy resolution of around 15% and a CR rejection factor of $\mathcal{O}(10^{-2})$ or better. Combined with the energy threshold of about 100 GeV and a high-energy effective area of some 10^5 m^2, this allows detection of sources of 1% of the strength of the Crab Nebula ($\nu F_\nu \sim 3\times10^{-13}$ erg cm^{-2} s^{-1} around

Figure 6

Four SNRs imaged in (dominantly) nonthermal X rays (*left*) and resolved in VHE γ-rays with HESS (*right*). (*a*) RX J1713.7 − 3946 with 1–3 keV data from ASCA (Uchiyama, Takahashi & Aharonian 2002), (*b*) RX J0852.0 − 4622 with ROSAT (1.3–2.4 keV) (Aschenbach 1998), (*c*) RCW 86 with 2–4 keV data from XMM-Newton (Vink et al. 2006), and (*d*) SN 1006 with Chandra archive data (0.5–10 keV). The HESS data are taken from Aharonian et al. (2006b, 2007d, 2009b) and Naumann-Godo et al. (2008). The white scale bars are 0.5° long.
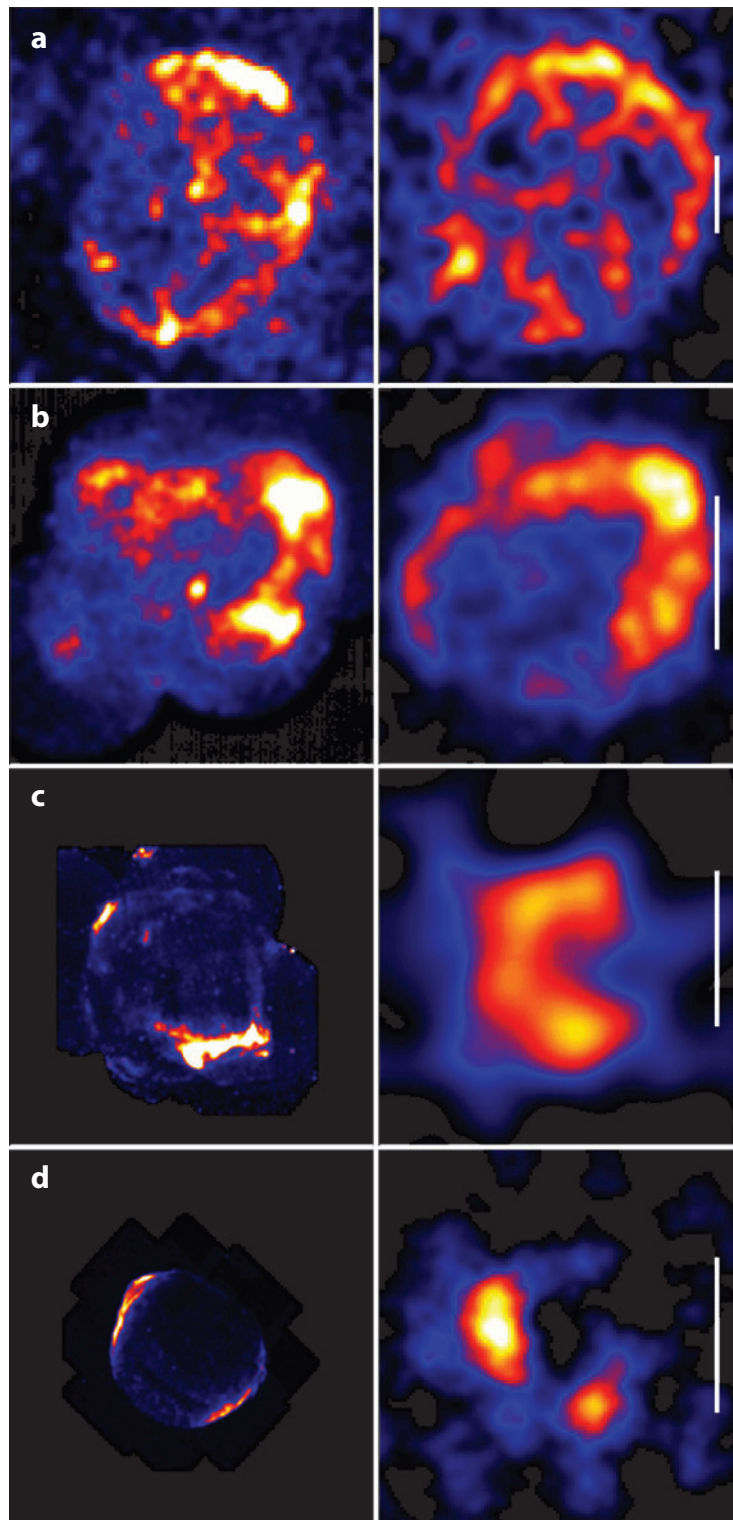
Table 1   Properties of selected air-Cherenkov instruments, including two of historical interest (*HEGRA* and *CAT*)

Instrument	Lat. (°)	Long. (°)	Alt. (m)	Tels.	Area (m²)	Pixels	FoV (°)	Thresh. (TeV)	Sens. (% Crab)
H.E.S.S.	−23	16	1800	4	428	960	5	0.1	0.7
VERITAS	32	−111	1275	4	424	499	3.5	0.1	1
MAGIC	29	18	2225	1	234	574	3.5†	0.06	2
CANGAROO	−31	137	160	3	172	427	4	0.4	15
Whipple	32	−111	2300	1	75	379	2.3	0.3	15
HEGRA	29	18	2200	5	43	271	4.3	0.5	5
CAT	42	2	1650	1	17.8	600	4.8†	0.25	15

†These instruments have pixels of two different sizes. Adapted from Hinton (2008).

1 TeV) within 25 h of observations close to Zenith. Performance of IACTs is at some point limited by fluctuations in air-shower development; for example, at energies below 10 GeV an air-shower is, in principle, still detectable, but because of the small number of Cherenkov-emitting particles, the energy determination is quite unreliable. Current instruments, however, are still relatively far from reaching fundamental limits; for example, shower fluctuations allow an angular resolution of a fraction of an arc-minute at TeV energies, provided that the number of Cherenkov photons detected is sufficient, and a CR rejection factor of order 10^{-4} at TeV energies (Hofmann 2006). A nontrivial issue in the analysis of data is the absolute energy calibration. Cherenkov light from local muons is often used to calibrate the response of instruments, but variations in atmospheric profile and transmission and of the orientation of the shower axis relative to the geomagnetic field can influence the shower development and the light yield (e.g., Bernlohr 2000) and cause systematic calibration uncertainties at the 10%–20% level.

3.3. Ground-Based Particle Detectors

The direct detection of air-shower particles offers a method of γ-ray detection with close to 100% duty cycle and very wide (∼1 steradian) field of view. Because of these advantages, this method offers an interesting complementary approach, despite the fact that the point-source sensitivity of such detectors is currently almost two orders of magnitude poorer than the most sensitive IACTs (at a few TeV). Indeed the extensive air-shower sampling (EAS) technique has recently produced its first contributions to the catalog of TeV sources (Abdo et al. 2007a) and proved its usefulness for all sky surveys (at modest sensitivity) and the detection of diffuse emission (Abdo et al. 2008).

The main challenges of the EAS approach are the rejection of the CR background and directional and energy reconstruction using the exponentially decreasing tail of particles detected well beyond shower maximum. High altitudes are therefore critical to achieve low (<1 TeV) thresholds with such instruments. In addition, although in principle all-sky detectors, the field of view obtained is limited in practice by the rapid increase in energy threshold with zenith angle; typically a factor two increase between 0° and 30° zenith (see, for example, Abdo et al. 2007a). The reconstruction of the primary γ-ray direction is based on shower front timing. The arrival time of the shower front can be determined with an accuracy of a few nanoseconds over ∼100 m baselines leading to typical resolutions of 0.3°–1° (e.g., Atkins et al. 2003). The much larger fluctuations present in the particle number at ground level with respect to the essentially calorimetric air-Cherenkov approach make primary energy determination extremely difficult for EAS detectors. The rejection of the hadronic background is based on the muon content of showers and/or the distribution of shower particles on the ground.

The Water Cherenkov approach pioneered by the MILAGRO collaboration appears to represent the most cost-effective method of achieving complete ground coverage. MILAGRO is a $80 \times 60 \times 8$ m pond instrumented with PMTs and surrounded by 175 water tanks, located at an altitude of 2630 m (Atkins et al. 2003). MILAGRO achieves its best background rejection power and sensitivity in the regime above 10 TeV. Widely spaced ($\sim$1 m^2 detectors $>$5 m apart) scintillation-based detectors have been used for CR measurements and in the search for UHE γ-ray sources for many years. Instruments of this type located at high altitudes can be used for γ-ray astronomy around a few TeV, as demonstrated with the Tibet Air-Shower Array (Amenomori et al. 1999) at 4300 m above sea level. The ARGO-YBJ instrument is a 5800 m^2 complete ground coverage instrument at the same site, utilizing resistive plate counters (RPCs) and achieving a threshold of a few hundred GeV and a sensitivity similar to that of MILAGRO. However, this approach is likely prohibitively expensive for a much larger area next-generation detector.

4. VERY-HIGH ENERGY γ-RAY SOURCES

As can be seen from **Figure 1a**, the TeV sky, despite a modest number of known objects ($\sim$80), contains a diverse collection of different object classes. Numerically dominant are the sources clustered along the plane of our galaxy (see **Figure 1b**). In contrast to GeV energies, sources, rather than diffuse emission, dominate our current view of the Galaxy. In the following, we summarize the important characteristics of each class of TeV γ-ray sources in the context of the discussion on particle acceleration, transport, and radiation given in Section 2. **Table 2** gives a summary of prominent Galactic VHE γ-ray emitters for which firm identifications exist. As there is insufficient space here for an adequate discussion of diffuse TeV emission, we refer the reader to Aharonian et al. (2008h) for a review of this topic and also the complex situation at the Galactic center.

Table 2   Selected galactic VHE γ-ray sources with well-established multiwavelength counterparts

Object	Type	Method	Flux	Reference
PSR B1259-63	Binary	Pos/Var	7*	Aharonian et al. (2005b)
LS 5039	Binary	Pos/Per	3*	Aharonian et al. (2006a)
LS I +61 303	Binary	Pos/Var	16*	Albert et al. (2006b)
RX J1713.7–39046	SNR	Mor	66	Aharonian et al. (2004)
Cassiopeia A	SNR	Pos	3	Aharonian et al. (2001)
Vela Junior	SNR	Mor	100	Katagiri et al. (2005)
RCW 86	SNR	Mor	5–10?	Aharonian et al. (2008)
SN 1006	SNR	Mor	?	Naumann-Godo et al. (2008)
Crab Nebula	PWN	Pos	100	Weekes et al. (1989)
G 0.9+0.1	PWN	Pos	2	Aharonian et al. (2005d)
MSH 15–52	PWN	Mor	15	Aharonian et al. (2005a)
HESS J1825-137	PWN	EDMor	12	Aharonian et al. (2006e)
Vela X	PWN	Mor	75	Aharonian et al. (2006g)

Note that all these objects are X-ray sources. Fluxes are approximate percentages of the TeV flux from the Crab Nebula; *indicates variable emission. The final column lists the publications where a firm identification of the source was made. These associations were established through a range of methods, given here in abbreviated form: *Pos*, the centroid position of the VHE emission is established with sufficient precision that there is no ambiguity as to the counterpart. *Mor*; there is a match between the γ-ray morphology and that seen at other wavelengths. *EDMor*; energy-dependent morphology is seen that approaches the morphology seen at other wavelengths at some limit, and is consistent with our physical understanding of the source. *Var*, γ-ray variability correlated with that in another waveband is observed. *Per*; periodicity in the γ-ray emission is seen, matching that seen at another wavelength. Table adapted from Hinton (2008).

4.1. Supernova Remnants

Ever since Zwicky (1939), supernova remnants have been viewed as the most likely sources of galactic cosmic rays up to an energy of at least that of the knee of the CR spectrum around 10^{15} eV, and possibly beyond 10^{17} eV. This argument is based in part on the energy input required to maintain the CR flux in the Galaxy, $dE/dt \approx \rho V \tau \sim 5 \cdot 10^{40}$ erg s^{-1}, with the energy density in cosmic rays $\rho \sim 1$ eV cm^{-3}, the confinement volume of cosmic rays $V \sim 10^{67}$ cm^3, and the characteristic residence time $\tau \sim 10^7$ year. With a kinetic energy output of 10^{51} erg per explosion and a rate of 2–3 per 100 years, an average of 10% of the supernova kinetic energy needs to be converted into CR energy. The first-order Fermi acceleration process outlined in Section 2.1, possibly enhanced by magnetic field amplification, provides a means to plausibly reach this efficiency and a maximum energy beyond 10^{15} eV, and naturally provides a power-law spectrum with an index around 2, which can explain the observed CR index if energy-dependent diffusion and escape are invoked (see, for example, Strong, Moskalenko & Ptuskin 2007). Although this scheme is generally accepted, there are still open questions concerning the consistency of required diffusion speeds and (the lack of a significant) anisotropy of the CRs at the Earth. Equally important, whereas the presence of high-energy electrons in SNRs can be inferred from the nonthermal X-ray spectra measured in several objects, modulo the a priori unknown, strength of B-fields, efficient acceleration of nuclei still lacks undisputed evidence, and observational proof is missing that acceleration in SNR can quantitatively account for the observed CR spectrum.

VHE γ rays trace the relevant populations of energetic particles in SNRs. The flux of hadronic γ rays is proportional to the CR density times the density of target gas, and the electronic IC γ rays directly trace the electron density, given that target photon fields are likely to be almost constant on the scale of the SNR. The ratio of IC γ rays and synchrotron X-rays is determined by the strength of the magnetic field. A detailed study of acceleration in an SNR shell, and distinction between the shell and the nebula of a possible pulsar created in the explosion, requires the shell to be resolved in VHE γ rays. This has so far been achieved for four SNRs: RX J1713.7−3946 (Aharonian et al. 2006b), RX J0852.0−4622 (alias *Vela Junior*) (Aharonian et al. 2007d), RCW 86 (Aharonian et al. 2009b), and, most recently, SN 1006 (Naumann-Godo et al. 2008). The γ-ray spectrum measured for RX J1713.7−3946 extends to several tens of TeV and follows a power law with index 2 up to about 20 TeV where a cut-off sets in (**Figure 7**), demonstrating the presence of primaries in the 100s of TeV energy range (Aharonian et al. 2007e). In all cases, there is a strong similarity between the morphology observed in VHE γ rays and in nonthermal X-rays, once the difference in PSF of the instruments is taken into account (see **Figure 6**). The correlation between X-rays and γ rays seems to argue in favor of a leptonic origin of γ rays. Correlation with gas density, as traced by CO, is less pronounced. This may, however, be due to a lack of resolution along the line of sight (i.e., in distance estimated by line velocity), making it difficult to know if a given gas mass is actually colocated with the accelerated particles. Only in a few special cases can the association between gas and remnant be proven by an observed high-velocity dispersion of the gas, resulting from the interaction with the SNR shock, or by OH maser emission.

The complex morphology of the remnants, with nonuniform emission along the rim, reflects their interaction with their environment and makes interpretation difficult, in particular given the lack of high-resolution, 3-dimensional information on the surrounding gas density. In the case of SN 1006, located off the Galactic plane in a less complex environment, the observed bipolar emission pattern can be modeled more easily: SN 1006 is believed to be threaded by a relatively uniform magnetic field, and nonthermal emission marks the polar caps where the B-field vector is roughly parallel to the expansion direction. In the equatorial regions, where field lines are perpendicular to the direction of shock propagation, particle injection into the Fermi process is
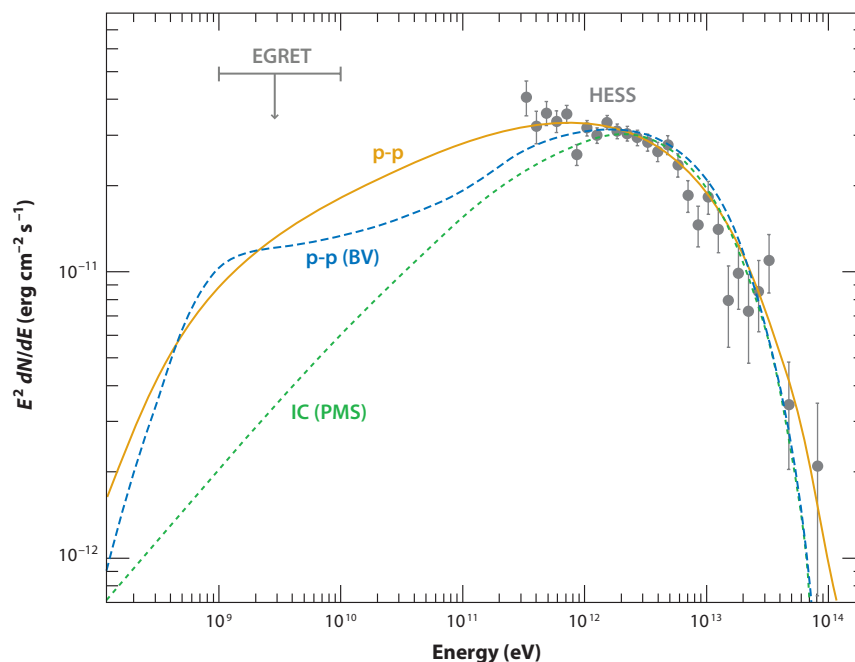
Figure 7

The SED of RX J1713.7−3946 at γ-ray energies. Three curves are shown in comparison to the dark gray
HESS data (Aharonian et al. 2007e) and EGRET upper limit: (*a*) the best-fit γ-ray spectrum arising from
interacting protons with an energy distribution following a power-law with exponential cut-off (see Kelner,
Aharonian & Bugayov 2006) (*solid orange line*), (*b*) hadronic emission as calculated by Berezhko & Völk
(2006) (*dashed blue line*), and (*c*) IC emission as calculated by Porter, Moskalenko & Strong (2006) (*dotted
green line*). Reproduced from Hinton (2009).

presumably inefficient, since particles spiral along field lines and are immediately overrun by the
shock. In the polar regions, injection is more effective, resulting in significant CR current and
most likely in turbulent magnetic field amplification, rendering the acceleration process even more
efficient.

Explaining the VHE emission from RX J1713.7−3946—probably the best-studied case—as IC
emission of electrons requires magnetic fields of around 10 μG (Aharonian et al. 2006b). These
magnetic fields are at variance with the significantly higher fields of at least 50 μG determined
from the width of X-ray emitting filaments, translated into an electron cooling time (e.g., Berezhko
& Völk 2006), and from the temporal variations observed in X-ray structures (Uchiyama et al.
2007), which directly measure the cooling time. Questions remain, though, on whether these high
magnetic fields are characteristic of the entire SNR, and if the observed structures are due to
variations in electron density rather than magnetic fields; only if this is the case, is an IC origin
of the γ rays firmly ruled out. There are no significant variations of γ-ray spectral shape across
the TeV SNRs, and the observed spectra are well described by hadron acceleration models that
generate a power-law distribution with an index close to 2, with a gradual high-energy cut-off
(**Figure 7**). Leptonic models tend to generate spectra that are too hard at low energy, reflecting
the fact that the index of IC γ rays is 1.5, for an electron index of 2 (see Section 2.2). This problem
can be solved to a limited extent by adjusting the composition of target radiation fields and by
introducing multi-zone models with different cut-offs, where different IC peaks are superimposed

to mimic an E^{-2} spectrum (e.g., Porter, Moskalenko & Strong 2006). In hadronic models, on the other hand, the strong X-ray/γ-ray correlation is nontrivial to obtain. In the case of high B-fields, electron lifetimes are comparable to acceleration timescales and the X-ray flux is influenced both by the energy input in accelerated electrons and by the strength of B-fields. Hadronic γ rays, on the other hand, reflect proton flux—which should scale with the (injected) electron flux—multiplied by the gas density. A strong correlation between X-rays and γ rays requires a link between gas density and B-field strength; magnetic field amplification (see Section 2.1) may provide a mechanism for this.

A final demonstration of CR origin in SNRs may be achieved by a combination of wider spectral γ-ray coverage, improved resolution or morphology, and larger-scale measurements of magnetic fields. Detection of neutrinos from SNRs would also demonstrate hadronic origin, but is challenging even for the largest instruments such as ICECUBE, and suffers similarly from the fact that, for a quantitative analysis, the target gas density needs to be known. Investigation of global CR energetics and spectra will in any case certainly require the γ-ray detection and spectral analysis of a representative sample of SNRs.

Another approach toward demonstrating CR acceleration in SNRs is to look for dense molecular clouds adjacent to, or interacting with, an SNR. In clouds, interactions of accelerated protons and nuclei will give rise to an enhanced γ-ray flux proportional to the cloud's mass (Equation 15), whereas IC radiation from electrons is not enhanced. Two candidate systems where this might be occurring are W 28 (Aharonian et al. 2008e) and IC 443 (Albert et al. 2007a) (**Figure 8**). W 28 is an old remnant (30–150 kyr) that has most likely released most of its CRs. VHE γ-ray data show four emission hot-spots coincident with enhancements of gas density; if interpreted as proton interactions in passive clouds, their masses imply a CR flux that is 10 to 30 times the flux near Earth, a plausible value given the proximity (at least in projection) of the remnant. A similar situation is seen in IC 443, where TeV emission coincides with a massive molecular cloud, with OH maser emission indicating that the SNR shock wave is hitting the cloud.
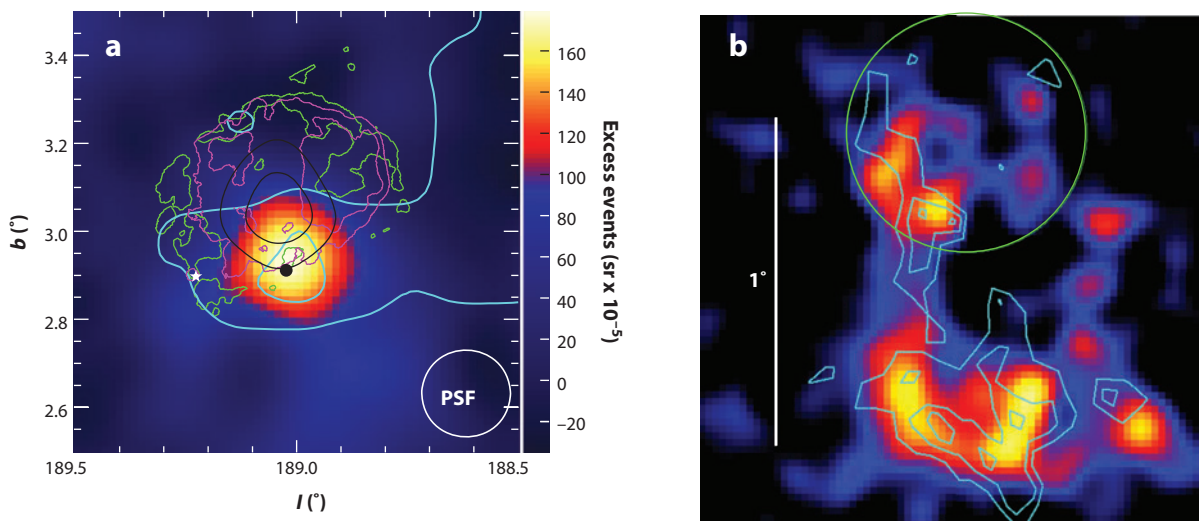

Figure 8

Multiwavelength views of IC 443 (*a*) and W 28 (*b*). Molecular tracer ^{12}CO (J $= 2 \rightarrow 1$) is shown (*cyan contours*) in comparison to TeV data (*color scale*) from HESS (Aharonian et al. 2008e) and MAGIC (Albert et al. 2007a).

4.2. Pulsars and Pulsar Wind Nebulae

The first VHE γ-ray source to be detected, the Crab Nebula (Weekes et al. 1989), is a pulsar wind nebula (PWN), where populations of electrons and positions with energies up to PeV energies emit X-rays and IC γ rays (e.g., Atoyan & Aharonian 1996). As PWNe have a well-defined central energy source and are typically close enough to be spatially resolved, they allow study of relativistic flows, and the shocks that result when these winds collide with their surroundings (Gaensler & Slane 2006). PWNe are the most abundant class amongthe sources discovered in the H.E.S.S. survey of the Galactic Plane. Many of the fundamental concepts concerning PWNe are summarized in the seminal papers by Rees & Gunn (1974) and Kennel & Coroniti (1984); for a recent summaries see Gaensler & Slane (2006).

A supernova explosion may create a pulsar, a neutron star with a magnetic field axis that is misaligned with the rotation axis. The rotating magnetic dipole will emit electromagnetic radiation at a luminosity $\dot{E} \sim 3{\cdot}10^{33} B_{12}^2 P_{\mathrm{ms}}^{-4}$ erg s^{-1} and will spin down; B_{12} is the surface magnetic field in units of 10^{12} G and P_{ms} the period in ms. Pulsars with γ-ray PWN tend to have $\dot{E}$ around and above 10^{35} erg s^{-1}. The time dependence of the spin-down energy loss is given by

$$\dot{E}(t) = \dot{E}_o/(1 + t/\tau)^p, \tag{16}$$

with $p = (n + 1)/(n - 1)$, with the characteristic spin-down time τ. For pure dipole radiation one has a *breaking index* $n = 2$ and $\tau \sim 10 P_{0,\mathrm{ms}}^2/B_{12}^2$ y where $P_{0,\mathrm{ms}}$ is the birth period of the pulsar; measured values for n lie between 2 and 3. The rotating field creates a voltage drop of order $10^{17} B_{12}/P_{\mathrm{ms}}^2$ V, which can be used to accelerate particles, fed by electron-positron pair cascades in the giant electric and magnetic fields near the pulsar surface. Accelerated electrons will emit γ-radiation, which appears pulsed to a stationary observer away from the rotation axis. Both the polar caps of pulsars and the "outer gap" at a couple of stellar radii have been considered as emission regions (see, for example, Harding 2007 for a review and references). Radiation emitted near the polar cap of the pulsar should cut off sharply at a few GeV because cascading in the high fields in this region prevents escape of higher-energy photons. In the region of the "outer gap," energies of tens of GeV may be reached.

The relativistic electron-positron wind from the pulsar terminates in a shock where the ram pressure of the wind is balanced by the pressure of the surrounding nebula. At the shock, the kinetic energy of the wind is transformed into random motion. Outside the shock, the resulting relativistic electron-positron gas will convect outward at subsonic speeds, $v < c/\sqrt{3}$, v decreasing initially as $1/r^2$, forming an expanding PWN visible in sychrotron radiation and IC γ rays. Assuming Bohm diffusion, convection of particles will dominate over diffusive propagation in most of the nebula (see, for example, de Jager & Djannati-Ataï 2008). The reverse shock created in the expanding SNR may collide with the expanding PWN after some kyr and may temporarily halt the expansion of the PWN. The evolution of PWNe is summarized, for example, in Blondin, Chevalier & Frierson (2001).

In retrospect, it appears plausible that PWN are dominant among galactic VHE γ-ray sources: The energy content of a PWN—of order 10^{49} erg—is small compared to the energy of $\sim 10^{51}$ erg dissipated in a supernova shock, but because a large fraction of the energy is carried by relativistic electrons with radiative lifetimes of 10^3–10^4 years (Equation 7), kinetic energy is very efficiently converted to radiation, compared to nuclei with interaction timescales of $\mathcal{O}(10^7$ years) (see Section 2.4). In addition, after $\mathcal{O}(10$ kyr), decelerating supernova shocks can no longer confine the highest energy particles, cutting off emission at VHE energies, whereas a powerful pulsar may drive a PWN significantly longer.

Because electrons suffer energy-dependent energy losses as they convect/diffuse away from the pulsar, both synchrotron X-ray and IC γ-ray spectra should evolve with increasing distance from the pulsar. Indeed, this is observed in X-rays for a number of PWN, and in a single object at TeV energies.

Table 2 lists γ-ray sources that are almost certainly associated with PWNe. Criteria for identification as a PWN include positional coincidence with a known pulsar powerful enough to potentially power the source, and the detection of an X-ray PWN. In some cases, a radio SNR shell is also present providing a potential contribution to the γ-ray emission. **Figure 9** shows some of the best γ-ray PWN candidates, with characteristics that were surprising at the time of discovery: (*a*) the large size of the γ-ray sources—typically $\sim$0.5°, corresponding to a few tens of parsecs for typical few kpc distances, sometimes an order of magnitude larger then the corresponding X-ray PWNe; and (*b*) the displacement of γ-ray sources from the pulsars by as much as the source radius, frequently putting the pulsar at the edge of the nebula. That the association is nevertheless significant can be demonstrated in two ways: A statistical study of sources in the H.E.S.S. Galactic Plane Survey shows a significant γ-ray excess near powerful pulsars (Carrigan et al. 2007) and in one case—HESS J1825−137—energy-dependent morphology is observed (Aharonian et al. 2006e), with the source shrinking toward the pulsar for higher-energy γ rays, as expected because of radiative cooling of electrons convecting away from the pulsar.

The difference in size between γ-ray PWNe and X-ray PWNe can be attributed to the difference in energy of the electrons responsible for the radiation. For inferred B-fields at the PWN core of some 10 µG, electrons of many tens of TeV are required to produce X-rays in the keV range (Equation 11). For these fields, cooling timescales are of order kyr, resulting in a modest range of particles. Electrons emerging from this inner region of the PWN still have energies sufficient to produce TeV γ rays in interactions with IR and optical photons in the KN regime (Equation 10), but in the assumed µG fields in the outer regions of the PWN the synchrotron peak is shifted into the optical, where it cannot be detected for all practical purposes. This also implies that VHE γ-ray emitting electrons, with characteristic cooling times of some 10 kyr, are accumulated over a much longer history of the pulsar, for medium-aged pulsars reaching back to the birth of the pulsar, where the energy output rate was one to two orders of magnitude higher. As a result, the γ-ray luminosity can reach and even exceed the current spin-down luminosity of the pulsar; an equilibrium is only reached once the pulsar age is large compared to cooling timescales, as is typically the case for X-ray emitting electrons. An example for a resulting SED is shown in **Figure 10** for the object HESS J1640−465 (Funk et al. 2007). In the model shown here, electrons, up to 20 kyr old are responsible for the detected VHE γ rays, with their synchrotron radiation peaking (undetectably) in the visible. Young electrons, recently injected into the PWN, generate the compact X-ray nebula seen with XMM-Newton.

Displacements between pulsars and their γ-ray PWNe appear to be fairly common, but their origin is not fully understood; at least in the two cases where the proper motion of the pulsar is known (Vela X and HESS J1825−137), the displacement between nebula and pulsar is almost orthogonal to the pulsar motion, eliminating the explanation that the pulsar was created with a significant kick, leaving a "relic" PWN behind. The origin of the displacement is most likely a consequence of the environment, with density gradients deforming the evolution of the SNR shell and hence also the PWN (Blondin, Chevalier & Frierson 2001). Alternatively, target photon fields for IC scattering may be enhanced locally due to stars or star clusters.

The sample of γ-ray PWNe is not large enough to systematically assess how PWN properties depend on pulsar properties. However, among the PWNe detected so far, two trends seem to emerge, with some caveats concerning selection bias (see, for example, Mattana et al. 2009):

Figure 9

Five γ-ray PWN candidates in X-rays (*left*) and TeV γ rays (*right*). (*a*) Vela X, (*b*) MSH 15−52, (*c*) the K3 and Rabbit PWNe in the Kookaburra Nebula, and (*d*) G18.0−0.7/HESS J1825−137. The γ-ray images are all made using HESS, see Aharonian et al. (2005a, 2006d, 2006e, 2006g). Publicly available X-ray data have been reprocessed to produce the X-ray images: (*a*) ROSAT, (*b*) Chandra, (*c*) XMM and Chandra (*white inset*), (*d*) XMM. The positions of the associated radio pulsars are shown with black crosses. The white scale bars are 0.5° long.
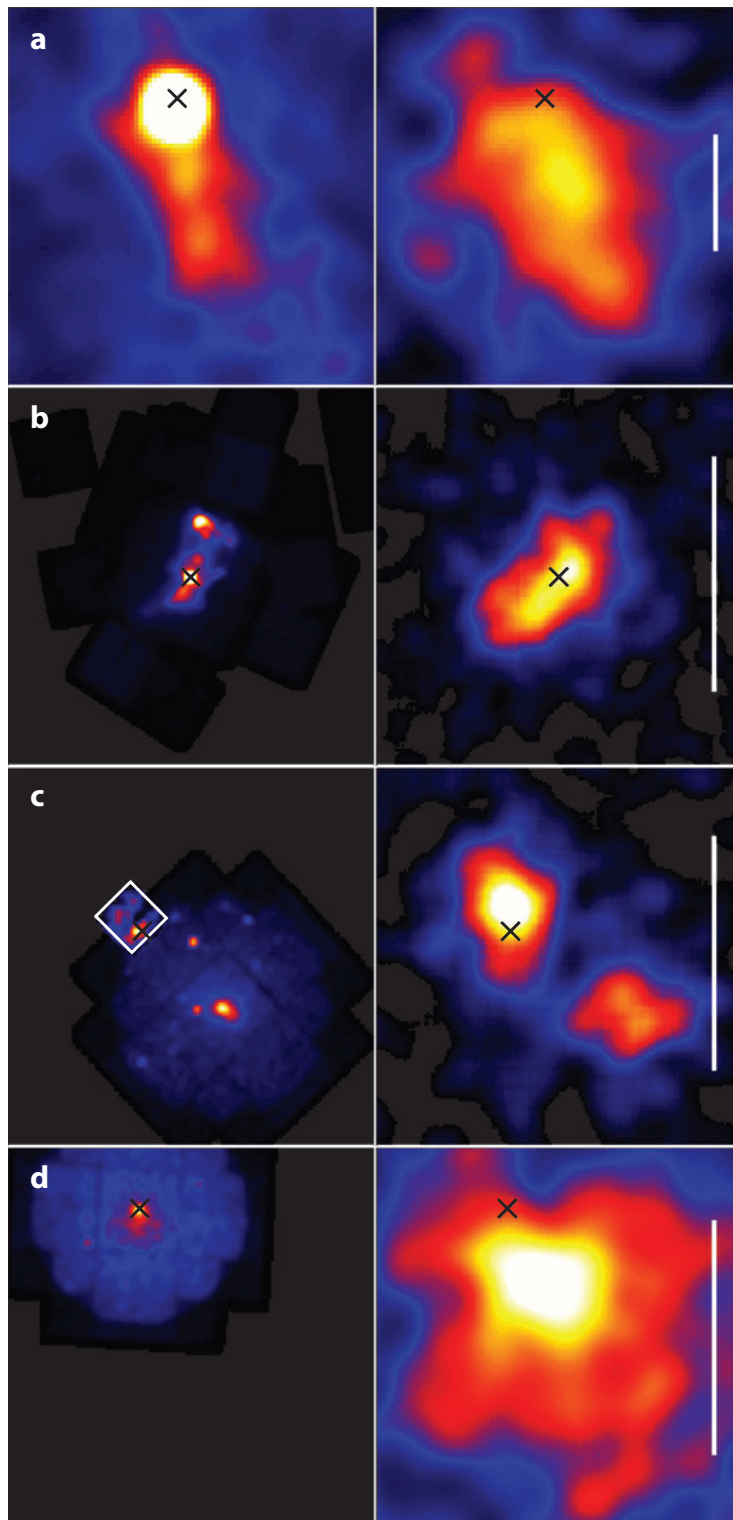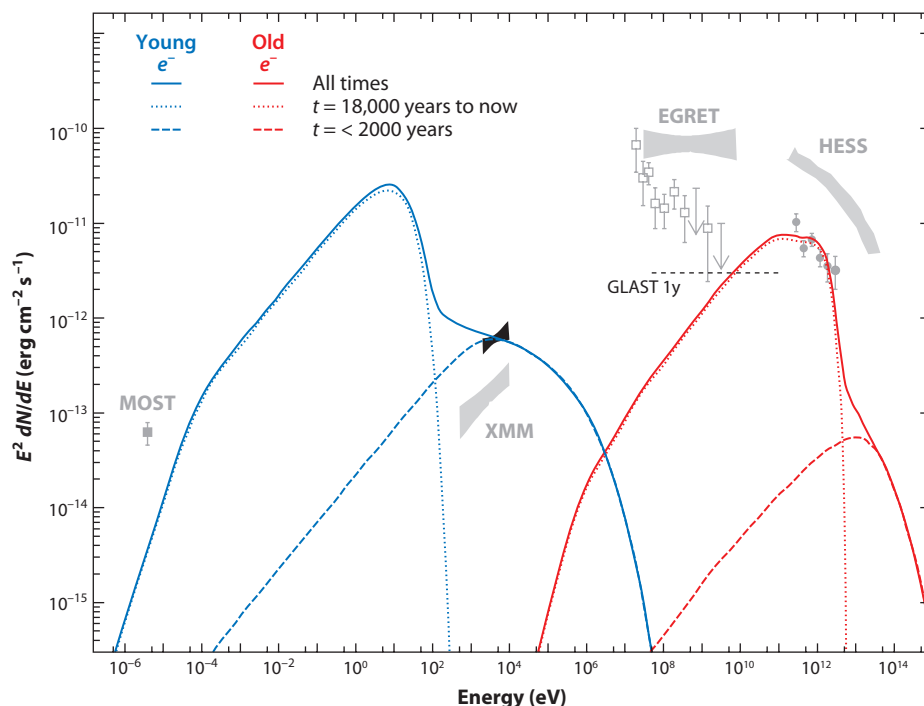
Figure 10

SED for HESS J1640−465, showing hypothetical contributions from young (*blue lines*)/old (*red lines*)
electrons. Data for HESS J1825−137 are shown for comparison (*gray regions*). Reproduced from Funk et al.
(2007).

(*a*) the ratio of γ-ray luminosity to spin-down loss tends to decrease with increasing spin-down
loss $\dot{E}$ (or decreasing pulsar age), and the fraction of energy radiated in X-rays increases, and (*b*) very
energetic pulsars (such as the Crab) tend to have very compact nebulae. A plausible explanation is
that for rough equipartition between particle energy and magnetic fields in the nebula, the fields
increase with $\dot{E}$, which implies that the ratio of X-ray to IC luminosities increases with $\dot{E}$ and that
the lifetime and range of electrons decrease. Furthermore, due to the strong correlation between
pulsar age and spin-down luminosity, high spin-down pulsars tend to be young, such that the
population of slower-cooled γ-ray emitting electrons is still increasing, whereas X-ray emitting
electrons have already reached their equilibrium output. The size of evolved γ-ray nebulae tends
to saturate at some 10 pc (**Figure 9**). This may be because the nebulae themselves are confined by
the ambient medium, or because radiative losses and convection timescales are such that multi-TeV
electrons die out.

By far the best-studied PWN is the Crab Nebula (Hester 2008). Its broad-band SED exhibits
overlapping synchrotron and IC spectra, the first extending from radio into the EGRET energy
range, the second from EGRET energies to ~100 TeV (**Figure 11**). Recently, the MAGIC collab-
oration succeeded in detecting, for the first time, a pulsed component in the VHE energy range,
above 25 GeV, hence excluding a pure polar-cap scenario as the origin of the pulsed emission (Aliu
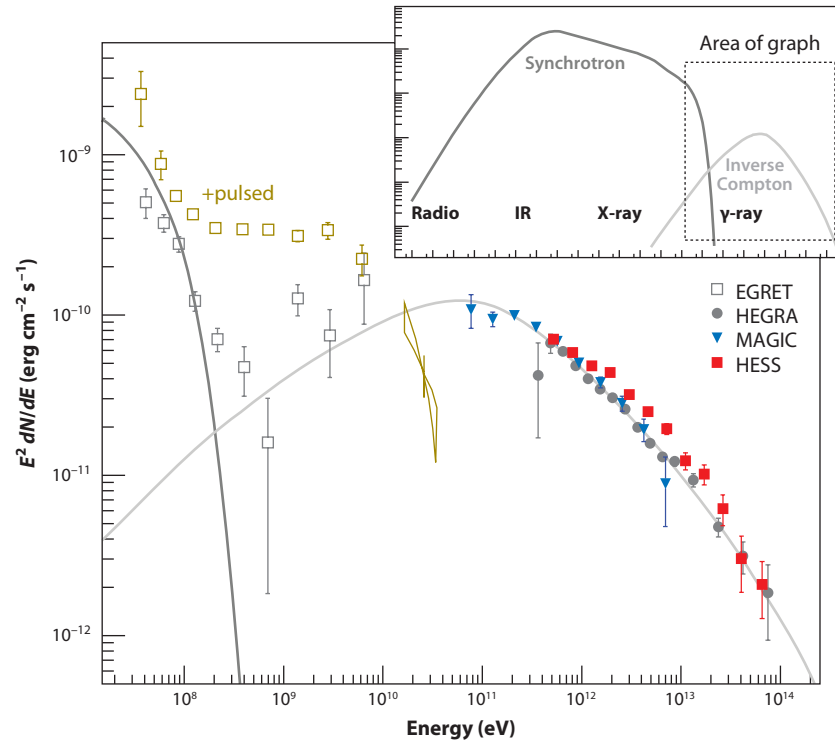et al. 2008).

Figure 11

The SED of the Crab nebula and pulsar, adapted from Hinton (2009).

4.3. Compact Object Binary Systems as γ-ray Sources

The physical environment inside a close binary system (or an eccentric binary close to periastron) is radically different from that of the diffuse ISM relevant to SNRs and PWN. This environment is characterized by very high radiation densities $\mathcal{O}(1 \text{ erg cm}^{-3})$ of rather high frequency photons $\mathcal{O}(1 \text{ eV})$ and high magnetic fields (mG–G). The consequence of this environment for relativistic electrons is that rapid cooling is inevitable. In the case where the radiation pressure dominates, the cooling of TeV electrons will occur in the KN regime, with implications for the spectral shape discussed in Section 2.2.

All relevant timescales in such a system are short in comparison to the length of observation programs (typically years), for example, the acceleration and cooling time for relativistic electrons and the orbital period. It is therefore expected that γ-ray emitting binaries will be variable point-like objects if electrons dominate the γ-ray production. Hadron accelerating binaries may produce steady and extended γ-ray emission if the protons and nuclei can escape the production region without significant energy losses. If γ rays are produced inside the binary system, then the assumption of free escape is normally invalid. In the presence of intense radiation fields, $\gamma-\gamma$ interactions produce e^+/e^- pairs that are likely to IC scatter, leading to electromagnetic cascades. This effect, combined with KN IC cooling, can lead to γ-ray spectral shapes radically different from those seen in diffuse sources (see, for example, Khangulyan, Aharonian & Bosch-Ramon 2008).

The most obvious energy source inside a binary system in which one member is a compact object (neutron star or black hole) is accretion. Particle acceleration in jets produced by accretion onto a

compact object is well established in extragalactic objects and in the early 1990s Galactic analogues to AGN were discovered and dubbed microquasars (Mirabel & Rodriguez 1994). The internal and external shocks associated with such jets provide potential sites for particle acceleration. The primary alternative power-source is the collision of stellar/neutron-star winds, with acceleration at the termination shock of the wind, in a compressed version of a PWN. Of the three well-established systems, one, PSR B1259−63/SS 2883, is unambiguously a binary PWN. For the other two systems (LS 5039 and LS I +61 303) both PWN and microquasar scenarios have been extensively discussed. These objects are briefly described below. Note that a much more complete historical account can be found in Aharonian et al. (2008h).

The most detailed TeV measurements so far exist in the case of LS 5039, a 3.9-day period system of a $\sim$20 $M_{\odot}$ (O6.5V type) star and a compact companion of mass $3.7^{+1.3}_{-1.0}M_{\odot}$ (Casares et al. 2005). **Figure 12** shows the flux and spectral index of the VHE emission of LS 5039 as a function of orbital phase, as measured using H.E.S.S. (Aharonian et al. 2006a). As the distance between
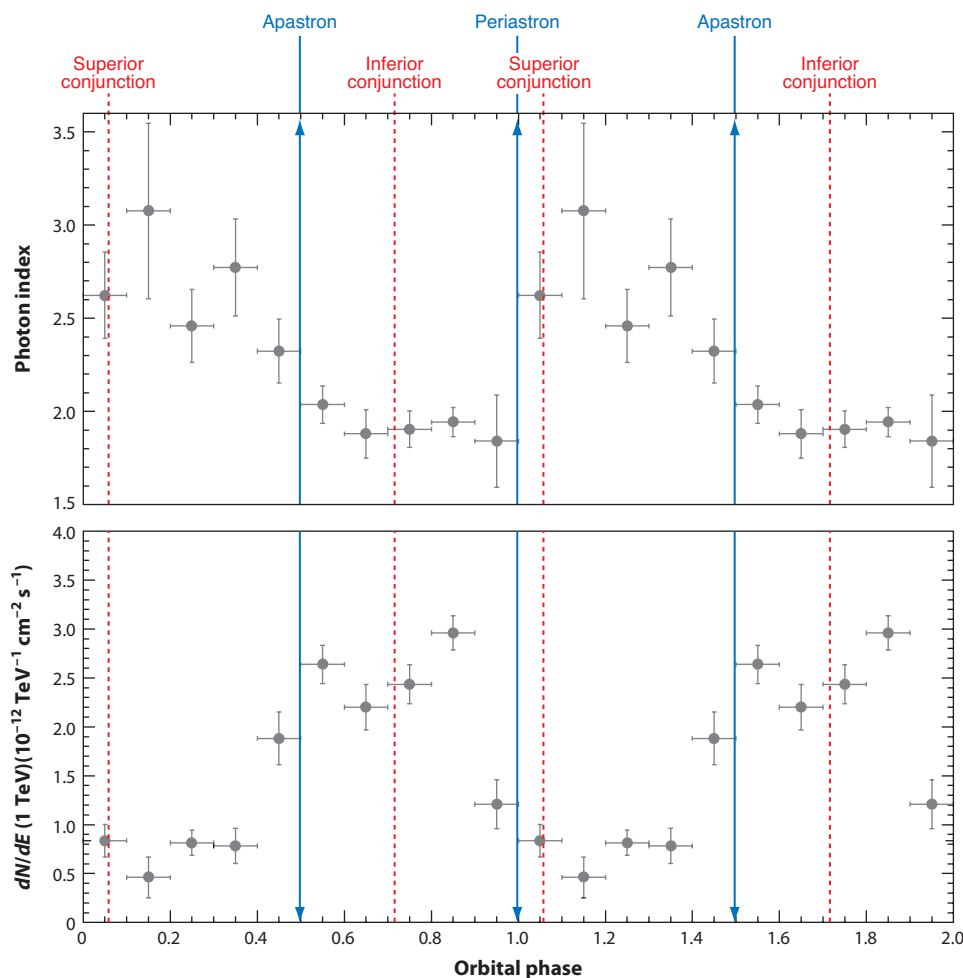

Figure 12

Phase-folded light curve and spectral index variations for the binary system LS 5039. Reproduced from Aharonian et al. (2006a).

the stars varies by a factor $\sim$2 around the orbit, the observed modulation of flux and spectrum with period is not unexpected. The maximum flux occurs at inferior conjunction, the point where $\gamma-\gamma$ absorption is expected to be at a minimum. However, the observed modulation is certainly not consistent with the simple-minded expectation for such absorption (and/or cascading). As discussed in Section 2.5, the peak absorption should occur at $0.9/E_{T,eV} = 300$ GeV (as the thermal photons from the companion star have $kT \approx 3$ eV), whereas there is apparently no modulation of flux at this energy. It seems likely that effects such as the angular dependence of the IC cross-section, adiabatic losses, and the dependence of acceleration efficiency (and also the efficiency of injection into the acceleration process) and maximum energy, on distance between the massive star and compact object (i.e., changing accretion rate, shock velocity...) must be taken into account, together with the geometry of the system, to reach an understanding of the physical processes at work. As LS 5039 appears to host a bipolar radio jet with a speed $\approx$0.2c (Paredes et al. 2000), the accretion powered microquasar scenario has been most extensively discussed, but despite extensive theoretical work (see Khangulyan, Aharonian & Bosch-Ramon 2008, and references therein) the acceleration site and nature of the compact object are still unclear in this system.

LS I +61 303 is a longer-period (26.5-day) system with a lower mass companion ($\sim$10 $M_\odot$, type B0Ve) which has been extensively observed by the MAGIC and VERITAS collaborations (see Albert et al. 2008c, and references therein). As in the case of LS 5039, VLBI radio observations had revealed extended jet-like radio emission in LS I +61 303, leading to its classification as a microquasar. However, more recent VLBI data from Dhawan, Mioduszewski & Rupen (2006) suggest that the radio structure rotates with orbital phase, as might be expected for the cometary emission of a shocked pulsar-wind encountering a (higher momentum) stellar wind from the massive companion.

In the remaining well-established γ-ray binary system, the pulsar nature of the compact object is well established by radio pulsation measurements. PSR B1259$-$63 and its B2e companion SS 2883 form a highly eccentric binary with an orbital period of $\approx$3.4 years (Johnston et al. 1992). TeV emission from the system close to its periastron passage was predicted by Kirk, Ball & Skjaeraasen (1999) and observed using H.E.S.S. (Aharonian et al. 2005b). PSR B1259$-$63 is powerful and close enough ($\dot{E} \sim 10^{36}$ erg s^{-1}, $d \approx 2.3$ kpc) that TeV emission might have been expected for a classical PWN. The TeV detection around periastron is usually attributed to the boost in IC emission from the strong radiation field of SS 2883.

The detection using the MAGIC telescope of a single flare from Cyg X-1 is extremely important as in this system there is no doubt about the nature of the compact object—it is a $21 \pm 8 \, M_\odot$ black hole. The $\approx$80-minute flare has a significance of approximately 4.1 σ after accounting for statistical trials (Albert et al. 2007d). At present there is therefore only strong evidence for, rather than proof of, VHE emission from Cyg X-1.

Given the relatively deep survey of most of the Galactic volume using H.E.S.S., it is natural to ask if additional candidates exist for γ-ray binary systems. Of the $\sim$20 unidentified VHE sources, very few are point-like in nature, as would be expected by analogy with identified sources. By far the best candidate for a new γ-ray binary is HESS J0632+057 (Aharonian et al. 2007f), a point-like TeV source coincident with a Be star and an EGRET source. Follow-up observations of this object with XMM-Newton led to the discovery of a variable X-ray source coincident with the star (Hinton et al. 2009). If all these objects are truly associated then the SED resembles that of the known γ-ray binaries. This discovery suggests that a population of γ-ray binaries exists with somewhat lower X-ray, radio, and γ-ray fluxes than the three well-established systems, which have so far escaped detection.

4.4. Stellar Clusters and Stellar Winds

All known Galactic sources of VHE γ rays are associated (directly or indirectly) with massive star formation. Both the end-points of the massive stellar lifecycles, SNRs and pulsars, and high-mass stars with compact companions (HMXBs) are TeV emitters. It is natural to consider whether massive stars can accelerate particles to TeV energies in the absence of a compact object. The idea of particle acceleration at the shock front formed by colliding stellar winds in a binary system of two massive stars has been developed over the past five years (see, for example, Benaglia & Romero 2003, Pittard & Dougherty 2006, Reimer, Pohl & Reimer 2006). The discovery of nonthermal hard X-ray emission from the massive binary Eta Carina (Leyder, Walter & Rauw 2008) has strengthened the case for high-energy particle acceleration in these systems.

So far there are no unambiguous VHE detections of individual colliding wind systems. However, extended TeV γ ray emission has been detected in and around Westerlund 2, the second largest concentration of massive young stars in our galaxy (Aharonian et al. 2007c). It seems plausible that this source is powered by the collective effect of stellar winds within the cluster. The association of massive stars Cyg OB2 has also been suggested as the counterpart of the unidentified Galactic plane source discovered using HEGRA (Aharonian et al. 2002). However, as essentially all known types of Galactic γ-ray source are associated (directly or indirectly) with high-mass star formation, it is plausible that these emission regions are associated with a single object within the cluster, such as a PWN, which has not yet been identified at other wavelengths, rather than the cluster as a whole.

4.5. Unidentified Very-High Energy γ-ray Sources

Roughly one third of the ∼60 Galactic TeV sources have no compelling counterpart at other wavelengths. In several cases, sensitive follow-up X-ray and radio observations have failed to identify these sources. Due to the apparent lack of emission of these TeV sources at lower frequencies, they are sometimes referred to as "dark accelerators." Two main questions arise for this population: (*a*) Do they represent a new class of objects, or are they members of the known classes? and (*b*) is the emission hadronic or leptonic in origin? The identified VHE sources have low-frequency counterparts with nonthermal emission usually attributed to the synchrotron process. The lack of synchrotron counterparts to the unidentified sources may be taken as a suggestion that the γ-ray emission is produced by hadrons rather than by leptons in most of these unidentified sources. However, there are several complications to this simple picture.

The distribution of sizes and spectra of the unidentified sources are rather similar to those of the identified sources. However, these properties may be common to most TeV sources on rather general physical grounds. For example, the relatively fast diffusion and slow energy losses of >TeV particles make TeV sources, in general, rather large. The expected size of an old (i.e., in equilibrium) source of electrons cooled by synchrotron emission and with Bohm diffusion is $r_{pc} \approx 30 B_{\mu G}^{1.5}$ (from Equations 1 and 7). Typical ISM magnetic fields of a few μG therefore lead to sources with a scale of a few parsecs, with apparent radii of ∼0.1° if located at typical distances of a few kpc. Unfortunately, the difficulty of identifying a source increases rapidly with its angular extent (unless closely matched in morphology to a bright object in another waveband, as in the case of the γ-ray SNR shells). The sensitivity of existing X-ray and radio surveys for very extended ∼0.5° objects is limited, and along the Galactic plane several candidates typically exist per degree of longitude. Source confusion can therefore be a major difficulty. Unidentified sources such as HESS J1745−303 (Aharonian et al. 2008c) lie in regions with a high density of candidates and very likely have unresolvable contributions from several objects. Even with better angular resolution the inherently diffuse nature of CR sources may make such regions very difficult to disentangle.

Leptonic scenarios for unidentified TeV sources are often dismissed as requiring very low magnetic fields to avoid bright synchrotron counterparts. However, even for $\mathcal{O}(10\,\mu\text{G})$ magnetic fields, it is plausible that the synchrotron emission accompanying the VHE IC emission is largely confined to the FIR–UV band, and hence almost impossible to detect for even the brightest sources (e.g., $\nu F\nu \sim 10^{-10}$ erg cm^{-2} s^{-1}) if they are extended on typical $\sim 0.2°$ scales. X-ray synchrotron emission with such B-fields requires higher electron energies than needed to produce the ~ 1 TeV IC γ rays. Furthermore, it is also possible to avoid radio counterparts if there is a low-energy cutoff in the injection spectrum of electrons, quite plausible in the case of, for example, pulsar wind nebulae. The lack of a radio counterpart may be harder to explain in the context of a hadronic scenario. Secondary electrons down to GeV energies are inevitably produced in the same p-p collisions that produce π^0 γ rays. The accumulation of these electrons (assuming an E^{-2} injection spectrum) will lead to a synchrotron energy flux

$$\nu F_{\text{sync}} \sim 3 \times 10^{-4}(\nu_{\text{GHz}})^{1/2}(B/10\mu G)^{3/2}(t/10^5\text{yr})\nu F_{\text{TeV}} \tag{17}$$

at intermediate energies where the low energy turnover in the electron distribution can be ignored and cooling is not important. In the saturated regime at high frequencies ($t_{\text{cool}} \ll$ age) the synchrotron energy flux is directly proportional to the γ-ray flux and $F_{sync} \approx 0.18 F_{\pi^0}$ (see **Figure 3**). For a typical TeV source with an energy flux of $\sim 10^{-12}$ erg cm^{-2} s^{-1}, the resulting extended X-ray source would be difficult to detect with current instruments.

In this context it is useful to consider some examples, both of sources that remain unidentified and those that were initially unidentified and now have likely counterparts. HESS J1303$-$631 (Aharonian et al. 2005c) is an example of a TeV source that originally appeared to be without any compelling candidate at lower frequencies. At the time of discovery, a PWN associated with PSR J1301$-$6305 was considered rather unlikely owing to the required extremely efficient conversion of spin-down power to TeV emission and the large offset and rms size of the TeV source (both $\approx 0.16°$). In light of the TeV PWN discoveries discussed in Section 4.2, PSR J1301$-$6305 is now considered a compelling candidate. Given an age of $\sim 10^4$ years, evolutionary effects are likely to enhance the TeV signal (see **Figure 10**). Furthermore, the pulsar is quite plausibly much closer than its nominal dispersion measure distance of 15 kpc, making the offset and size very typical for a TeV PWN.

The second class of no-longer unidentified objects contains those where follow-up observations have led to the discovery of new pulsars, PWN, and/or SNRs. HESS 1813$-$178 is an example of such an object, rapidly established as a new composite SNR following its discovery, based on new and archival data from the VLA, INTEGRAL, XMM, and Chandra (see Helfand et al. 2007, and references therein). HESS 1813$-$178 is, however, an unusual case. It is a rather bright ($\approx 3 \times 10^{-12}$ erg cm^{-2} s^{-1}), compact ($\approx 2'$) TeV source with a bright X-ray counterpart (AX J1813$-$178). Such rapid assignment to an existing source class seems unlikely for the remaining unidentified sources. **Figure 13** shows four example VHE sources for which there are no plausible candidates at lower frequencies. All lie within half a degree of the Galactic plane and all are significantly extended beyond the instrumental PSF.

4.6. Active Galaxies

The galaxy Mrk 421 was the second VHE γ-ray source detected (Punch et al. 1992); the number of extragalactic VHE sources has now risen to well over 20, with redshifts up to 0.536 (3C 279, Albert et al. 2008b). In order of increasing redshift, the VHE γ-ray emitters include M 87 ($z = 0.004$), Mrk 421 ($z = 0.030$), Mrk 501 ($z = 0.034$), 1ES 2344+514 ($z = 0.044$), Mrk 180 ($z = 0.045$), 1ES 1959+650 ($z = 0.047$), PKS 0548$-$322 ($z = 0.069$), BL Lacertae ($z = 0.069$),
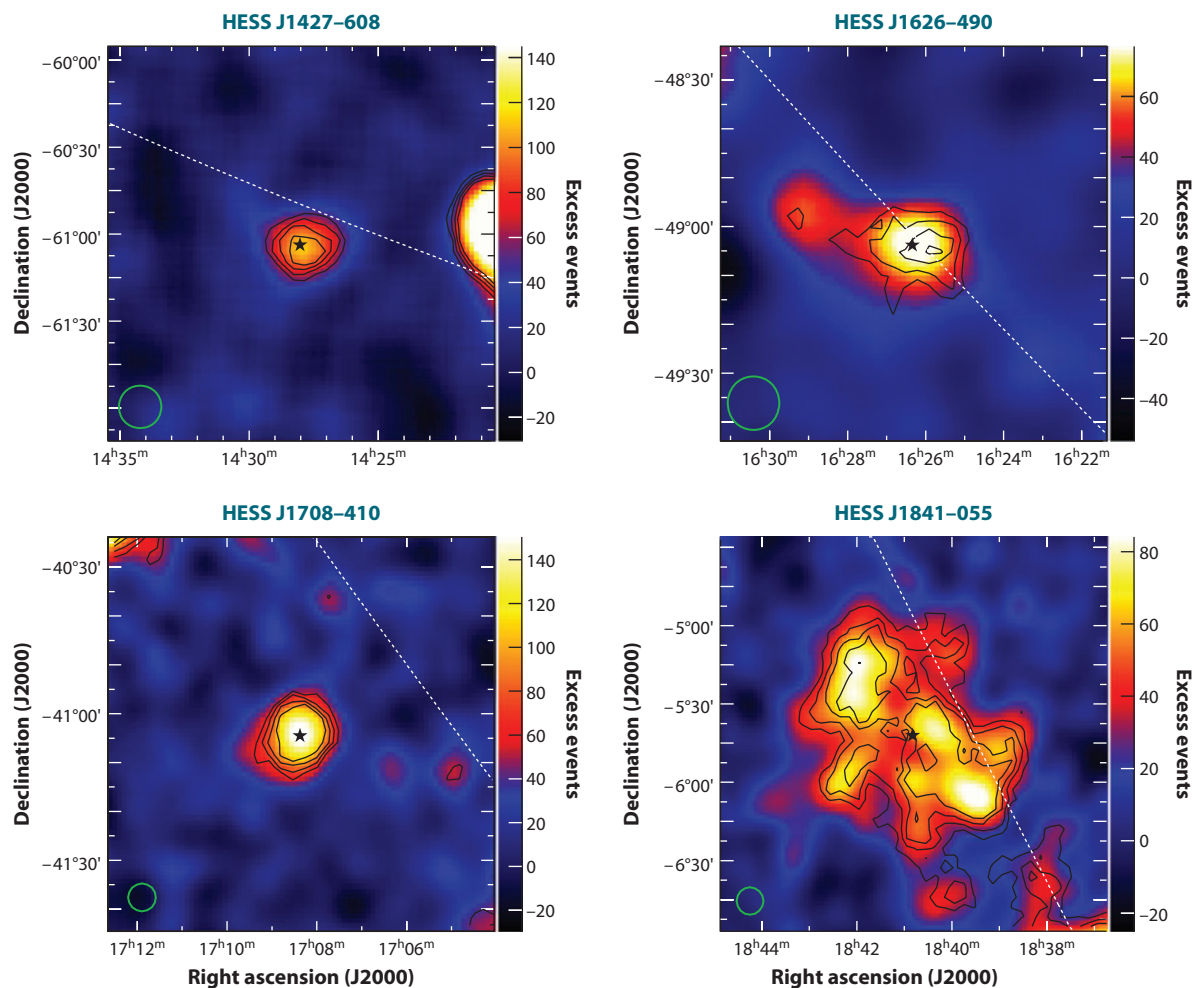
Figure 13

Selected unidentified γ-ray sources as seen by HESS The Galactic plane is shown as a white dashed line. The smoothed PSF is indicated by a green circle at the bottom-left of each image. See Aharonian et al. (2008d) for details.

PKS 2005−489 ($z = 0.071$), RGB J0152+017 ($z = 0.08$) (Aharonian et al. 2008b), W Comae ($z = 0.102$) (Acciari et al. 2008), PKS 2155−304 ($z = 0.116$), H 1426+428 ($z = 0.129$), 1ES 0806+524 ($z = 0.138$) (Acciari et al. 2008), 1ES 0229+200 ($z = 0.139$), H 2356−309 ($z = 0.165$), 1ES 1218+304 ($z = 0.182$), 1ES 0347−121 ($z = 0.188$), 1ES 1101−232 ($z = 0.186$), 1ES 1011+469 ($z = 0.212$), 3C 279 ($z = 0.536$), PG 1553+113 (z unknown). A compilation of emission characteristics and remaining references for these objects can be found in Wagner (2008). All these objects harbor Active Galactic Nuclei (AGN), where a supermassive black hole with a mass from millions to billions of solar masses accretes matter and powers jets—collimated highly relativistic outflows. Unlike Galactic VHE sources, all objects appear point-like given the ~5′ resolution of IACTs, and all VHE source positions are consistent with the nominal location of the AGN. With the exception of the radio galaxy M 87 (Aharonian et al. 2006f), all belong to the blazar class where a jet points toward the observer. High-frequency peaked BL
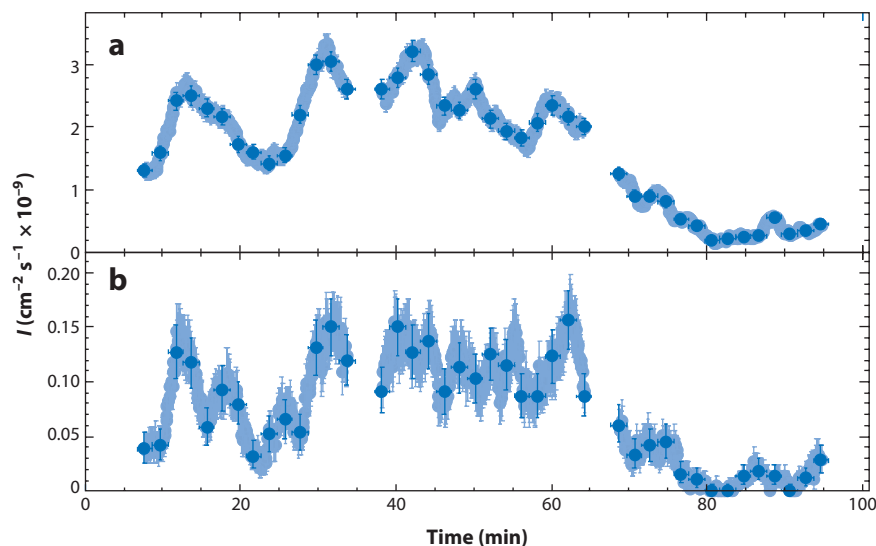
Figure 14

VHE light curve of PKS 2155−304 during the July 2006 flare, in two energy bands: 200–800 GeV (*b*) and above 800 GeV (*a*) (Aharonian et al. 2008a). The light curve is sampled in two-minute intervals around each point.

Lac objects (HBLs) dominate the sample. The few exceptions are the flat spectrum radio quasar (FSRQ) 3C 279, the intermediate-frequency peaked BL Lac object (IBL) W Comae, and the low-frequency peaked BL Lac object (LBL) BL Lacertae itself. Some objects—most notably Mrk 421 (e.g., Fossati et al. 2008) and PKS 2155−304 (e.g., Aharonian et al. 2007b; see **Figure 14**) exhibit burst-like variability on timescales of a few minutes to a few tens of minutes; emission from AGN such as M 87 or 3C 279 appears variable on day timescales. Despite the vastly larger distances, some AGN, at the peak of flares, outshine the strongest galactic sources by more than a factor of 10. Although low-statistics measurements of VHE blazar spectra are consistent with power laws, well-measured spectra are generally significantly curved, steepening with increasing energy, for example Mrk 421 (Krennrich et al. 2001) and PKS 2155−304 (Aharonian et al. 2007b). Spectral indices tend to increase with source distance, at least partly due to absorption of high-energy γ rays on infrared intergalactic photon fields (see Section 4.7), but perhaps also related to the fact that distant AGN must be intrinsically brighter to be detectable. Spectral indices vary with flux for some sources, with a tendency for spectra to harden with increasing activity (see Krennrich et al. 2002). All VHE-detected blazars are also relatively strong radio and X-ray sources; in fact, observation targets are typically selected on the basis of their output in these bands (Costamante & Ghisellini 2002). Optical measurements have also proven useful in tagging high-activity states of AGN for targeted observations by VHE instruments (see, for example, Albert et al. 2006a). The broad-band spectral energy distributions of AGN exhibit a double-humped shape, with a high-frequency peak in the GeV to TeV regime, and a low-frequency peak in the optical to X-ray regime (**Figure 15**). Simultaneous measurements in the X-ray and VHE γ-ray bands reveal, with a few exceptions (Daniel et al. 2005), strong correlations between the X-ray and γ-ray fluxes (e.g., Fossati et al. 2008), suggesting a common electron population as the origin of the radiation, with synchrotron X-ray emission and inverse Compton γ-ray emission. Similarly, average X-ray and γ-ray luminosities show a pronounced correlation (Wagner 2008).
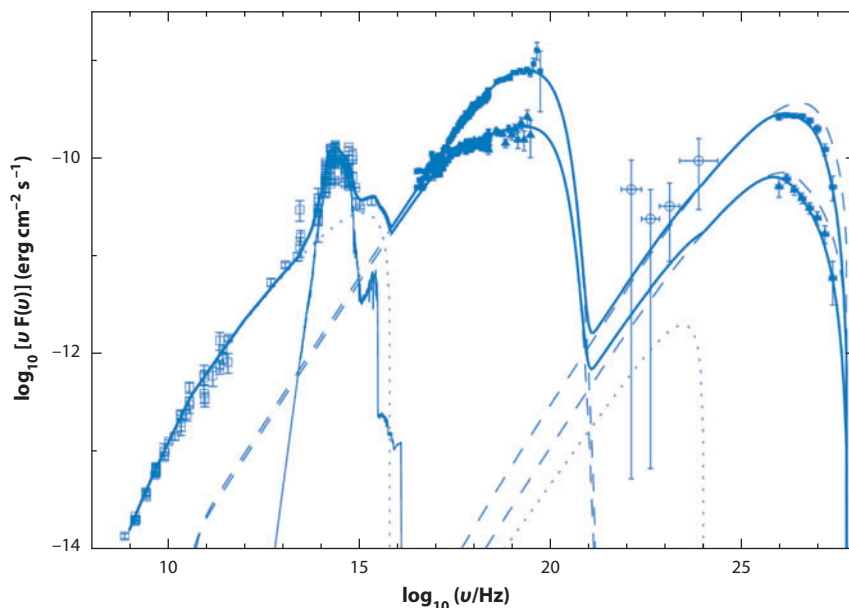
Figure 15

Spectral energy distribution of Mrk 501 in two different states (Katarzyński, Sol & Kus 2001). The two dominant peaks are interpreted as synchrotron and synchrotron self Compton (SSC) emission of electrons (*dashed lines*). Modeling of the SED at lower frequencies adds contributions where external photons are Compton-scattered (*dotted lines*) and emission by the host galaxy (*thin full line*).

In these blazars, VHE γ-ray emission is thought to arise inside the jets; models typically assume a spherical blob of high-energy particles moving along the jet axis, with flares created when high-energy electrons are freshly injected into the blob (e.g., Tavecchio, Maraschi & Ghisellini 1998). The relativistic motion of the blob beams and boosts the emission and reduces power requirements by a factor δ^4, with δ denoting the Doppler factor $\delta = (\Gamma(1 - \beta \cos\theta))^{-1}$, where Γ is the Lorentz factor describing bulk motion of the jet and θ is the angle between jet and observer. The blob size is usually estimated by causality arguments from the minimum timescale t_{var} of variability, $R \approx c t_{var} \delta$. Minimum Lorentz factors are then obtained from the requirement that the energy density in the blob rest-frame must be low enough to make the blob reasonably transparent for γ rays (e.g., Dondi & Ghisellini 1995), and are in the range of 10 to almost 100. Magnetic fields in the blob, as well as parameters of the electron spectrum, can then be determined from the relative spacing and height of the two peaks of the SED and from the requirement that the cooling time of electrons matches the flare timescale, and are typically in the range 0.01 G to 1 G. For the shape of the electron spectrum, a broken power law is frequently employed. Parameter estimates should, however, be viewed with caution; well-sampled AGN light curves are composed of a range of Fourier components with a red-noise spectral distribution (e.g., Aharonian et al. 2007b), without a highest frequency which could be unambiguously associated with the size of a blob. In Synchrotron-Self-Compton (SSC) models (e.g., Tavecchio, Maraschi & Ghisellini 1998) synchrotron photons generated in the blob provide the dominant target for IC up-scattering by electrons, resulting to first approximation in a quadratic increase of γ-ray flux with electron number and X-ray flux. Detailed modeling of broad-band spectra, however, also indicates the relevance of external target radiation components from other regions of the jet and

from the high-temperature gas surrounding the central engine (e.g., Katarzyński, Sol & Kus 2001) (**Figure 15**).

Phenomenological models frequently leave open how particles in the blob are accelerated; possibilities include shock-wave acceleration in MHD turbulence in the jet, centrifugal acceleration of particles along rotating magnetic field lines near the base of the jet, or shear (Rieger & Mannheim 2002). However, X-ray observations show that acceleration of high-energy particles must occur along the jet, since travel times from the base of the jet to X-ray emitting knots exceed cooling times. Many fundamental aspects of AGN jets and of particle acceleration in these jets are poorly understood, including the mechanisms that launch the jets and their composition. Not even the character of the emitting particle populations is firmly established: cascades induced by high-energy protons (see, for example, Mannheim 1993) can successfully reproduce most features of AGN SEDs, with the possible exception of very fast variability, which is hard to model owing to the long energy loss timescales of protons in comparison to electrons. VHE measurements are a promising method for probing jet properties and ultimately studying the environment of supermassive black holes.

The discovery of VHE γ-ray emission from M 87 established radio galaxies as a new class of source where γ rays are emitted at significant angles to the jet, not relying on Doppler boosting (and hence only observable for nearby objects). The observation of fast day-scale variability of the emission (Aharonian et al. 2006f, Albert et al. 2008a) excludes the extended jet or the radio lobes as sources and implies a compact emission region with a size comparable to the radius of the SMBH at the center of M 87, most likely the nucleus itself or possibly the knot HST-1 in the inner jet.

4.7. Probing Background Radiation Fields with γ rays

The energy spectra of extragalactic γ-ray sources are modified by interactions with the diffuse extragalactic background light (EBL, see Hauser & Dwek 2001 for a review;, see Section 2.5 and **Figure 4**). Because the absorption cross section peaks near threshold, there is an approximate mapping between the wavelength of an absorbing EBL photon and the energy of an interacting γ ray, $E_{\text{TeV}} \approx 0.7\lambda_{\mu m}$. The level of the EBL, in particular at the relevant IR wavelengths, is very difficult to determine by direct observation, because of overwhelming foreground light sources, hindering the interpretation of AGN spectra due to the uncertain correction for EBL absorption. On the other hand, the EBL is important in its own right, and the information provided by this TeV absorption is potentially very useful. The EBL represents the integrated, red-shifted emission from all epochs of the evolution of the Universe. The EBL, with its peaks around 1 μm from starlight and around 100 μm due to starlight reprocessed by dust (**Figure 16**), has embedded within it information on the history of galaxy and star formation in the Universe. Assuming "plausible" shapes for blazar spectra, one can use absorption features in γ-ray spectra to constrain the level and spectral distribution of the EBL (Stecker, de Jager & Salamon 1992). The plausible assumptions usually include a γ-ray spectral index $\Gamma_\gamma \geq 1.5$ at the source, and emitted spectra that are power laws, possibly curved with the index increasing, but not decreasing, with increasing energy. These assumptions are supported by nearby sources, which are less affected by EBL absorption. However, it cannot be firmly excluded that the more distant sources used to "measure" the EBL are subject to a selection bias and differ in their intrinsic spectra (e.g., Stecker, Baring & Summerlin 2007). EBL deabsorption with an optical depth $\tau(E)$ transforms a measured γ-ray flux $\Phi_o(E)$ into an intrinsic flux at the source $\Phi_i(E) = \Phi_o(E)e^{\tau(E)}$. A rapid increase of $\tau(E)$ at higher energies, as predicted in some EBL scenarios, will decrease the intrinsic spectral index and may conflict with the assumptions concerning intrinsic spectra. Sources with higher redshifts and
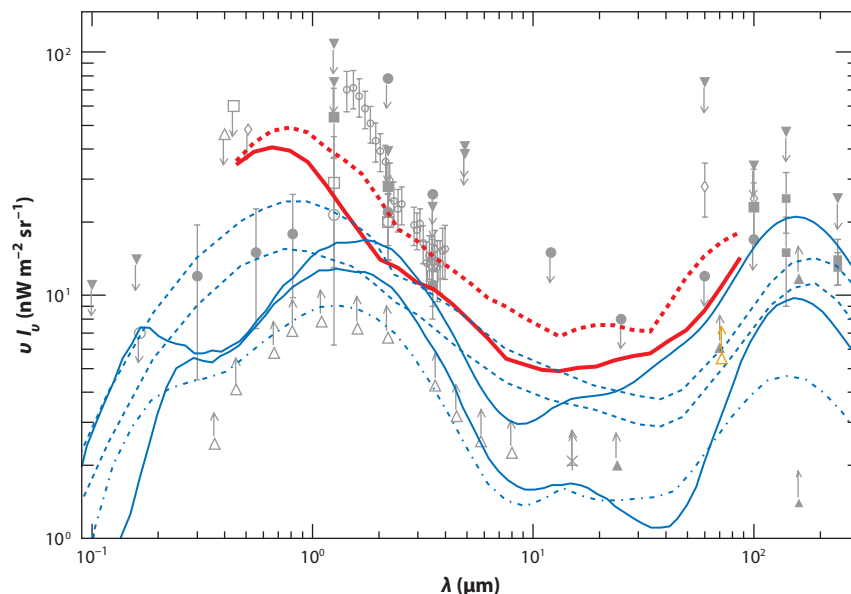
Figure 16

EBL limits obtained from VHE γ-ray spectra using plausible assumptions for intrinsic spectra (*thick red line*), compared to lower limits from direct observations—potentially hampered by incomplete subtraction of foreground emission—and including recent EBL models. The gray symbols are a collection of EBL measurements assembled by Mazin & Raue (2007, and see their figure 1 for definitions and references).

correspondingly large $\tau(E)$ and with hard measured spectra and wide energy coverage will provide the most stringent constraints. On the basis of spectra measured for 1ES 1101−232 ($z = 0.186$) and H 2356−309 ($z = 0.165$), upper limits for the EBL density at optical/near-IR wavelengths were derived that were within a factor 1.5 of the lower limits provided by the integrated light of resolved galaxies, and below the EBL level previously assumed (Aharonian et al. 2006c). Strong constraints on the shape of the EBL spectrum in the 5–10 μm region were obtained based on the spectrum of 1ES 0229+200 ($z = 0.139$) (Aharonian et al. 2007a). The dection of VHE γ rays from 3C 279 ($z = 0.536$) (Albert et al. 2008b) provided another demonstration of low EBL levels and hence the relatively high transparency of the Universe to γ rays. Limits derived for the EBL density often include—beyond the assumptions on intrinsic source spectra—certain minimal assumptions about the shape of the EBL spectrum itself. Mazin & Raue (2007) have developed an approach where arbitrary EBL shapes are tested and constrained, confirming earlier EBL limits (**Figure 16**). EBL determinations using absorption of VHE γ rays have driven development of models for EBL formation, and the latest models (see Franceschini, Rodighiero & Vaccari 2008) and calculations, based on hierarchical structure formation and employing detailed models for galaxy formation and evolution and the reprocessing of starlight by dust, reproduce the low EBL levels measured (see, for example, Primack, Gilmore & Somerville 2008).

4.8. Other Extragalactic Source Classes

A range of extragalactic objects beyond AGN is expected to emit VHE γ rays at some level, such as normal galaxies, starburst galaxies, galaxy clusters, GRBs, and the sources of ultrahigh-energy cosmic rays (UHECR); most of these are predicted to emit at a level not far below the sensitivity of current instruments, and many of these classes raise interesting new science topics.

4.8.1. Nearby galaxies. Diffuse γ rays from nearby normal galaxies are produced in CR interactions with the interstellar medium; their detection, combined with estimates of supernova rates in these galaxies, would allow concepts of CR acceleration and propagation in galaxies to be tested. Expected fluxes are discussed in Pavlidou & Fields (2001), applied to the EGRET energy range. However, detection of local group Galaxies at VHE energies will be difficult even for next-generation instruments.

4.8.2. Starburst galaxies and ultraluminous infrared galaxies. Starburst galaxies with strongly enhanced supernova rates and enhanced gas density, and their more extreme cousins the ultralumious infrared galaxies, should provide VHE γ-ray fluxes not far below current sensitivities, providing another test of concepts of CR acceleration. Among the best candidates are NGC 253 (Domingo-Santamaría & Torres 2005) and M 82 (Persic, Rephaeli & Arieli 2008); in fact, NGC 253 was claimed as a TeV emitter by the CANGAROO collaboration (Itoh et al. 2003), but this detection was not confirmed by later, more sensitive, observations with H.E.S.S. and CANGAROO (Itoh et al. 2007). Bounds on emission from the ultralumious infrared galaxy Arp 220 have been reported by the MAGIC collaboration (Albert et al. 2007b).

4.8.3. Galaxy clusters. Clusters of galaxies are the largest gravitationally bound systems in the Universe, and should contain a significant nonthermal particle population, fed by particle acceleration in accretion shocks during the assembly of the cluster, by supernova activity in cluster galaxies, and by particle acceleration by cluster AGN (e.g., Blasi, Gabici & Brunetti 2007; Völk, Aharonian & Breitschwerdt 1996). The time required for CRs to diffuse out of a cluster is generally supposed to be larger than the age of the Universe. As a consequence, the CR abundance in clusters provides a measure of the time-integrated CR production rate, and the CR spectrum is not softened by escape as it is, for example, inside our own galaxy. VHE γ-ray flux limits have been derived using the Whipple telescope for the Perseus and Abell 2029 clusters (Perkins et al. 2006), limiting the CR energy density to as little as 8% of the thermal energy density in the case of the Perseus cluster, depending on assumptions concerning the distribution of CRs relative to gas in the cluster. Such a value is well within the range estimated for different acceleration mechanisms, indicating that detections may be possible in the near future.

4.8.4. Gamma-ray bursts. Gamma ray bursts, GRBs, are usually explained by fireball models, with emission produced by relativistic shocks (e.g., Meszaros 2006). Both prompt and delayed γ-ray emission at GeV and TeV energies has been predicted (e.g., Asano & Inoue 2007, Pe'er & Waxman 2005), due to both leptonic and hadronic mechanisms. No VHE γ rays have been detected from GRBs so far. Truly simultaneous observations are primarily possible with wide-field instruments such as MILAGRO (see Abdo et al. 2007b, for limits on 17 GRBs), at the expense of sensitivity and energy threshold in comparison to current Cherenkov telescopes. In one case— GRB 060602B, an unusually soft GRB occurred in the field of view of ongoing observations of the H.E.S.S. telescope, although without giving rise to a detectable signal (Aharonian et al. 2009a). Upper limits were reported, for example, from the MAGIC collaboration for 9 GRBs (Albert et al. 2007c), with observations starting as early as 40 s after the burst, due to the fast slewing capabilities of the MAGIC telescope. A strong and nearby GRB, observed rather promptly, is needed to challenge GRB models. None of the limits obtained so far fall in this class, and patience will likely be required to obtain a VHE γ-ray detection of a GRB, even if a TeV emission component is present, due to the limited duty cycle and redshift reach of the sensitive instruments. An in-depth discussion and detailed references concerning high-energy γ rays from GRBs is given in Buckley et al. (2008b).

4.8.5. Sources of UHECR. Nearby accelerators of ultra high-energy cosmic rays (UHECRs)—within the $\approx$100 Mpc GZK radius—should also be sources of VHE γ rays. First, interactions during the propagation of UHECR beyond the GZK cut-off give rise to cascades feeding energy down to the TeV range (see Ferrigno, Blasi & de Marco 2005). Second, VHE photon production during acceleration of UHECRs is expected in some scenarios (see Levinson 2000). Again, fluxes for sources from which a few UHECR are detected are typically expected to lie at the lower edge of the sensitivity of current instruments.

5. VHE γ RAYS AND ASTROPARTICLE PHYSICS

The areas of VHE γ-ray astronomy discussed so far concern primarily issues in astronomy and astrophysics. The development of VHE γ-ray instrumentation has also been driven to a significant extent by questions in the field of astroparticle physics, above all the indirect search for dark matter. Results obtained by VHE instruments also have relevance to fundamental physics, for example in tests for an energy dependence of the speed of light, as predicted in some models of quantum gravity. The former aspect is addressed in more detail, the latter rather briefly.

5.1. Searching for Dark Matter

In the standard cosmological model (e.g., Frieman, Turner & Huterer 2008), which has emerged over the past decade, only about 4% of the energy density in the Universe is in the form of baryons, about 25% is cold dark matter (DM) and the remainder is dark energy. Evidence for the gravitational effects of DM is observed on all scales ranging from galaxies, where flat rotation curves require that visible matter is embedded in extended DM halos, to clusters of galaxies. DM is essential in explaining structure formation in the Universe, driving the formation of potential wells in which baryonic matter accumulates, forming galaxies. Structure formation favors cold dark matter, i.e., DM in the form of nonrelativistic particles, since rapidly streaming DM would have smoothed inhomogeneities in the matter distribution on small scales. Some form of weakly interacting massive particle (WIMPs; Steigman & Turner 1985) is required to explain the existing observations.

Creation and annihilation of DM particles was in equilibrium in the early Universe, but under the rapid expansion of the Universe the WIMP component was rapidly frozen out, the small interaction cross section no longer sustaining sufficient annihilation rates. The current DM abundance emerges naturally assuming typical weak interaction cross sections and WIMPs in the mass range of some tens of GeV to TeV. Candidates include supersymmetric particles, where the lightest supersymmetric particle is stable owing to (assumed) R-parity conservation, and Kaluza-Klein particles arising in theories with TeV-scale extra dimensions. As a result of gravitationally driven structure formation, DM particles form halos in which galaxies are embedded, with pronounced peaks at galactic centers. Simulations of structure formation predict a $1/r$ (NFW) density profile near the center of galaxies, with a significant number of subhalos scattered elsewhere within galaxies. However, details of the merger history of halos/galaxies as well as the influence of central black-hole formation may significantly influence the distribution of DM, resulting in large uncertainties in the predicted densities.

Identification of the nature of DM constituents (e.g., Hooper & Baltz 2008) has been a major theme of particle and astroparticle physics in the past one to two decades. Possibilities for the detection of cosmological DM include challenging direct-detection experiments, where DM particles—typically assumed to have a local density of around 0.3 GeV cm^{-3}—scatter off nuclei, resulting in keV-scale recoil energies (Gaitskell 2004). Annihilation of DM particles in the
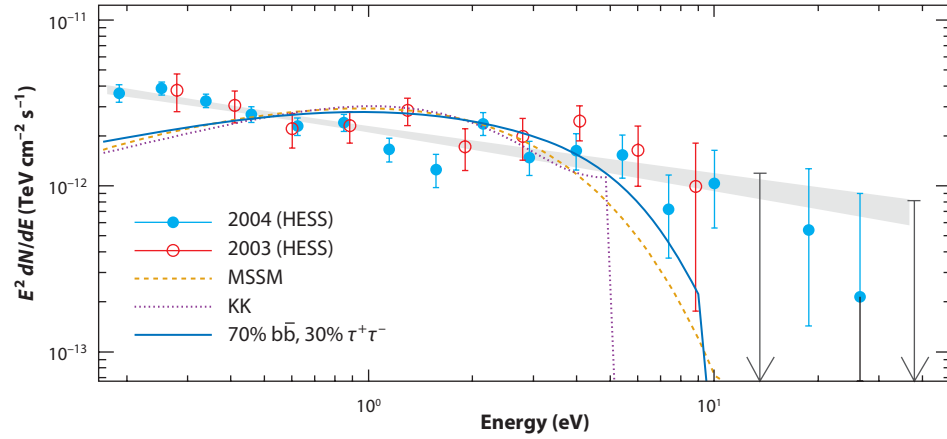
Figure 17

Spectral energy distribution from DM annihilation compared to the spectrum of γ rays from the Galactic center as measured using HESS Annihilation of "typical" 14 TeV WIMPs (*dashed line*): mix of 70% $b\bar{b}$ and 30% $\tau^+\tau^-$ modes of 10 TeV WIMPs (*solid line*): annihilation of 5 TeV KK particles (*dotted line*) (Aharonian et al. 2006h).

galactic vicinity of the Sun will enhance CR electron and positron fluxes and in particular the positron/electron ratio, as well as the antiproton/proton ratio, depending on the specific annihilation channels. Finally, and most relevant for VHE γ-ray astronomy, annihilation of DM particles will generate an enhanced γ-ray flux from regions of high DM density, the annihilation rate reflecting two-particle interactions, proportional to the square of the density (see Buckley et al. 2008a, and references therein). γ rays may be produced directly in the primary annihilation process, by the decay of hadrons created via annihilation into fermion-antifermion pairs or vector bosons, or by IC scattering of electrons created in the annihilation or in the decay chains of annihilation particles. γ rays from DM annihilation are identified by their spectral and directional signature. The expected flux is generally written as a product of a "particle physics" factor and an "astrophysics" factor,

$$\Phi_\gamma = \left(\frac{\langle \sigma v \rangle}{M^2} D_\gamma(E) \right) \left(\frac{1}{4\pi} \int_{LOS} \rho^2 dl \right), \qquad (18)$$

where $\langle \sigma v \rangle$ is the velocity-weighted annihilation cross section of WIMP particles of mass M, $D_\gamma(E)$ the spectral yield per annihilation, and ρ the density of DM particles, with the annihilation flux being proportional to the line-of-sight (LOS) integrated squared density. For all decay modes the spectrum $D_\gamma(E)$ cuts off at the mass of the DM particles, which annihilate effectively at rest. The spectral details depend very much on the decay modes. Two-body decays into γ rays, such as $\gamma\gamma$ or $Z^0\gamma$ or $H\gamma$, resulting in a monoenergetic line signature, are possible via loop processes, but are strongly suppressed in most scenarios. Dominant decays into quark-antiquark pairs or boson pairs, followed by hadronization and hadron decays, generate a broad featureless spectrum with an SED hump at about 10% of the WIMP mass (see **Figure 17**). Decays into tau leptons result in a harder γ-ray continuum. In one class of models, two-body decays are helicity suppressed, boosting diagrams with internal Bremsstrahlung such as $W^+ W^- \gamma$ and a γ-ray enhancement near the kinematic limit (Bringmann, Bergström & Edsjö 2008), almost equivalent to line emission given the finite energy resolution of VHE γ-ray detectors (**Figure 18**).

The expected flux of annihilation γ rays is proportional to the LOS integrated squared DM density. Searches for signatures of DM annihilation in the VHE regime therefore concentrate
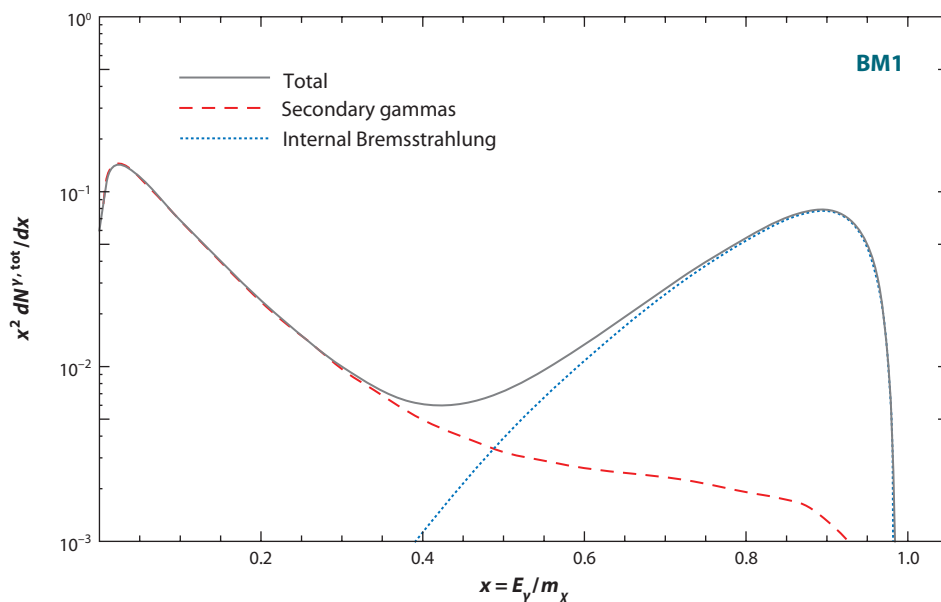
Figure 18

γ-ray spectrum resulting from DM annihilation in one of the benchmark scenarios of Bringmann, Bergström & Edsjö (2008), with strong contributions from internal Bremsstrahlung.

on objects with spikes in DM concentration. Favorable objects include the Galactic center, dwarf spheriodal galaxies such as Draco, Ursa Minor and Ursa Major, or Willman 1 (Strigari et al. 2008) as well as microhalos and DM enhancements predicted around intermediate-mass black holes (IMBHs) in the Galactic vicinity (Bertone, Zentner & Silk 2005), globular clusters, and supermassive black holes in external galaxies. A DM signal would have to be identified by a combination of spectral and directional signatures, with nearby sources exhibiting a narrow spike toward the center of the source combined with an extended tail.

In the VHE domain, despite extensive searches, no DM candidate source has been identified so far. In fact, predicted fluxes tend to be well below the sensitivity of current instruments, requiring "boost factors" of several orders of magnitude to make signals detectable, arising from enhancements in the DM density. Detection of a DM signal from the most obvious candidate source, the Galactic Center, is hampered by the presence of a strong astrophysical source of γ rays, responsible for a power-law spectrum of γ rays extending beyond 10 TeV, which may hide a faint low-energy annihilation signal. Limits on annihilation fluxes have been obtained, for example, for the Galactic Center (Aharonian et al. 2006h), the dwarf galaxies Draco (Albert et al. 2008d, Wood et al. 2008), Ursa Minor (Wood et al. 2008) and Sagittarius (Aharonian et al. 2008f), for local group galaxies (Wood et al. 2008) and for the globular cluster M15 (Wood et al. 2008), DM annihilation around IMBHs in the Galactic halo predicts detectable fluxes even in the absence of large additional boost factors (Bertone, Zentner & Silk 2005) and limits restricting the model parameter space have been obtained (Aharonian et al. 2008g), but the process relies on a specific astrophysical scenario which may not be realized in nature. DM annihilation fluxes from IMBHs depend only weakly on the annihilation cross-section, since close to an IMBH the DM density is so high that annihilation limits the peak density, so that the resulting $\rho^2\sigma$ varies only as $\sigma^{2/7}$.

5.2. Violation of Lorentz Invariance and Quantum Gravity

In the framework of quantum gravity models, Lorentz invariance may be violated such that the propagation speed of radiation depends on the photon energy and possibly on its helicity (see, for example, Amelino-Camelia et al. 1998). For energies small compared to the scale of quantum gravity, the photon speed c' can be parametrized as

$$c' = c \left(1 + \xi \frac{E}{E_P} + \zeta \frac{E^2}{E_P^2} \right), \tag{19}$$

where $E_P = 1.22 \cdot 10^{19}$ GeV is the Planck energy and ξ and ζ are free parameters that are expected to be of order unity, unless specific symmetries forbid the corresponding terms; for example, there are classes of models with $\xi = 0$. GRBs and flares from AGN can be used to perform "time-of-flight" studies, searching for an energy dependence of the peak time of arrival of the emission. The best sensitivity in terms of limits on ξ and ζ is obtained for short bursts with well-located peak emission, for distant objects and for large energy differences. A positive detection of energy-dependent peak emission could of course also be attributed to mechanisms inside the source, where such effects can arise rather naturally, governed by acceleration and/or cooling timescales. To confirm that detection implies violation of Lorentz invariance, one would need to demonstrate that the effect increases with source distance, and that the distance dependence cannot be attributed to evolution of the source population. At VHE energies, the technique was first applied by the Whipple group to a flare of Mrk 421 ($z \approx 0.03$) (Biller et al. 1999), resulting in a limit of $|\xi| < 200$. More recently, MAGIC reported an energy dependence in the peak position of a flare of Mrk 501 ($z \approx 0.03$), finally quoting a limit $|\xi| < 60$ (Albert et al. 2008e). In the giant flare of PKS 2155 − 306 ($z \approx 0.12$) detected using H.E.S.S., no energy dispersion was visible, resulting in $|\xi| < 17$ (Aharonian et al. 2008a). VHE γ-ray observations are hence beginning to probe energy-scales up to a few % of the Planck energy. Although such time-of-flight measurements provide the most model-independent tests of a possible energy dependence of the speed of light, alternative methods, which make some additional assumptions, are significantly more sensitive, providing limits from $|\xi| < 10^{-7}$ for helicity-dependent speed modifications (e.g., Fan, Wei & Xu 2007) down to $|\xi| < 10^{-14}$ (e.g., Galaverni & Sigl 2008) based on decay kinematics.

6. CONCLUSIONS

VHE γ-ray astronomy can now legitimately claim to be a mature astronomical discipline, with resolved source morphologies and well-sampled light curves and energy spectra. Furthermore, as some objects have their peak energy output in the TeV range, VHE observations are clearly critical to our understanding of some astronomical objects. The primary success of the field so far is in the unambiguous identification of sites of cosmic particle acceleration. TeV photons are currently the only effective probe of relativistic hadrons in astrophysical environments. Two complementary techniques exist for ground-based γ-ray astronomy: IACTs and ground-based particle detectors. Both have significant further potential, with order-of-magnitude more sensitive instruments such as CTA and HAWC being planned. The IACT technique has the potential to cover the energy range from 10 GeV to hundreds of TeV, with an angular resolution of better than $1'$ achievable at a few TeV. Together, the Fermi satellite and IACTs will soon provide unbroken sensitive coverage over 7 orders of magnitude in γ-ray energy.

The number of VHE γ-ray sources is now over 80. More importantly, many different source types are represented. Supernova remnants and pulsar wind nebulae appear to dominate the Galactic population, but pulsed magnetospheric emission from the Crab pulsar has now been

detected from the ground and a number of binary systems have been established as TeV emitters. There is also TeV emission apparently associated with clusters of massive stars, perhaps as a consequence of stellar wind interactions. Variable emission from active galactic nuclei dominates the extragalactic TeV sky. A complex mixture of different mechanisms appears to be at work in these TeV sources. Bulk flow appears to be the main energy source; relativistic jets/winds in AGN/pulsars and nonrelativistic shocks driven by supernovae ejecta. Acceleration processes transfer energy from these bulk motions into populations of relativistic particles with power-law energy distributions. The convection, diffusion, and cooling of these particles then determine the properties of the high-energy radiation. For accelerated hadrons cooling does not usually modify the injection spectrum and the observed γ-ray spectral shape is close to that of the injected hadrons—possibly with modifications due to energy-dependent propagation. The situation for electrons is more complex, cooling can in general not be neglected, and there is a balance between synchrotron and IC losses; complex spectral shapes can emerge, particularly in the case of IC dominated cooling.

Galactic TeV sources are typically extended on 10 pc scales. Compact γ-ray sources require both compact accelerators and dense compact target material/radiation fields/magnetic fields, and such objects appear to be rare—with binary systems as the only established example. The cooling time for 10 TeV electrons in 10^{-5} G magnetic fields is $\sim10^4$ years—comparable to the active lifetime of the dominant sources, energetic pulsars, and young SNR. Both bulk motion at 1000 km s^{-1} over this timescale, and Bohm diffusion of electrons in older (cooling limited) objects, naturally produce 10 pc scale TeV sources. For sources on this scale the detection sensitivity of IACTs is very competitive with that of X-ray telescopes for detection of synchrotron counterparts.

The current extragalactic TeV sources are characterized by relativistic bulk motion and compact regions of acceleration and cooling, leading to variability on timescales down to minutes. For the blazar class, the boosting associated with this bulk motion allows us to see distant objects—with a current redshift record of 0.536. The combination of TeV data with observations of optical to X-ray synchrotron emission promises to be a powerful probe of the inner jets of these AGN. Extragalactic TeV sources also provide a useful tool to study the cosmic infrared background and fundamental physics such as the potential violation of Lorentz invariance at high energies.

The next decade of TeV astronomy should bring the source count to $\mathcal{O}(1000)$ and increase the diversity of known Galactic and extragalactic sources. Predicted VHE fluxes for several classes of astrophysical object are close to detectability with current instruments, for example, clusters of galaxies, starbursts, and GRBs. The indirect detection of Dark Matter is a major objective of the field, and considerable phase-space is available for discovery via this channel. For known source classes, more sensitive and precise observations will bring improved understanding, in particular a quantitative understanding of Galactic CR origin seems within reach of the next generation of IACT detectors. To conclude, TeV astronomy has emerged as a powerful tool for high-energy astrophysics and looks set to become our primary window on the nonthermal universe in the years to come.

DISCLOSURE STATEMENT

ACKNOWLEDGMENTS

LITERATURE CITED

Abdo AA, Allen B, Aune T, Berley D, Blaufuss E, et al. 2008. *Ap. J.* 688:1078–83

Abdo AA, Allen B, Berley D, Casanova S, Chen C, et al. 2007a. *Ap. J.* 664:L91–94

Abdo AA, Allen BT, Berley D, Blaufuss E, Casanova S, et al. 2007b. *Ap. J.* 666:361–67

Acciari V, Aliu E, Arlen T, Bautista M, Beilicke M, et al. 2009. *Ap. J.* 690:L126–29

Acciari VA, Aliu E, Beilicke M, Benbow W, Böttcher M, et al. 2008. *Ap. J.* 684:L73–77

Aharonian F, Akhperjanian A, Barrio J, Bernlöhr K, Börst H, et al. 2001. *Astron. Astrophys.* 370:112–20

Aharonian F, Akhperjanian A, Beilicke M, Bernlöhr K, Börst H, et al. 2002. *Astron. Astrophys.* 393:L37–40

Aharonian F, Akhperjanian AG, Aye KM, Bazer-Bachi AR, Beilicke M, et al. 2005a. *Astron. Astrophys.* 435:L17–20

Aharonian F, Akhperjanian AG, Aye KM, Bazer-Bachi AR, Beilicke M, et al. 2005b. *Astron. Astrophys.* 442:1–10

Aharonian F, Akhperjanian AG, Aye KM, Bazer-Bachi AR, Beilicke M, et al. 2005c. *Astron. Astrophys.* 439:1013–21

Aharonian F, Akhperjanian AG, Aye KM, Bazer-Bachi AR, Beilicke M, et al. 2005d. *Astron. Astrophys.* 432:L25–29

Aharonian F, Akhperjanian AG, Barres de Almeida U, Bazer-Bachi AR, Becherini Y, et al. 2008a. *Phys. Rev. Lett.* 101:170402–7

Aharonian F, Akhperjanian AG, Barres de Almeida U, Bazer-Bachi AR, Behera B, et al. 2007a. *Astron. Astrophys.* 475:L9–13

Aharonian F, Akhperjanian AG, Barres de Almeida U, Bazer-Bachi AR, Behera B, et al. 2008b. *Astron. Astrophys.* 481:L103–7

Aharonian F, Akhperjanian AG, Barres de Almeida U, Bazer-Bachi AR, Behera B, et al. 2008c. *Astron. Astrophys.* 483:509–17

Aharonian F, Akhperjanian AG, Barres de Almeida U, Bazer-Bachi AR, Behera B, et al. 2008d. *Astron. Astrophys.* 477:353–63

Aharonian F, Akhperjanian AG, Barres DeAlmeida U, Bazer-Bachi AR, Behera B, et al. 2009a. *Ap. J.* 690:1068–73

Aharonian F, Akhperjanian AG, Bazer-Bachi AR, Behera B, Beilicke M, et al. 2007b. *Ap. J.* 664:L71–74

Aharonian F, Akhperjanian AG, Bazer-Bachi AR, Behera B, Beilicke M, et al. 2008e. *Astron. Astrophys.* 481:401–10

Aharonian F, Akhperjanian AG, Bazer-Bachi AR, Beilicke M, Benbow W, et al. 2006a. *Astron. Astrophys.* 460:743–49

Aharonian F, Akhperjanian AG, Bazer-Bachi AR, Beilicke M, Benbow W, et al. 2006b. *Astron. Astrophys.* 449:223–42

Aharonian F, Akhperjanian AG, Bazer-Bachi AR, Beilicke M, Benbow W, et al. 2006c. *Nature* 440:1018–21

Aharonian F, Akhperjanian AG, Bazer-Bachi AR, Beilicke M, Benbow W, et al. 2006d. *Astron. Astrophys.* 456:245–51

Aharonian F, Akhperjanian AG, Bazer-Bachi AR, Beilicke M, Benbow W, et al. 2006e. *Astron. Astrophys.* 460:365–74

Aharonian F, Akhperjanian AG, Bazer-Bachi AR, Beilicke M, Benbow W, et al. 2006f. *Science* 314:1424–27

Aharonian F, Akhperjanian AG, Bazer-Bachi AR, Beilicke M, Benbow W, et al. 2006g. *Astron. Astrophys.* 448:L43–47

Aharonian F, Akhperjanian AG, Bazer-Bachi AR, Beilicke M, Benbow W, et al. 2006h. *Phys. Rev. Lett.* 97:221102

Aharonian F, Akhperjanian AG, Bazer-Bachi AR, Beilicke M, Benbow W, et al. 2007c. *Astron. Astrophys.* 467:1075–80

Aharonian F, Akhperjanian AG, Bazer-Bachi AR, Beilicke M, Benbow W, et al. 2007d. *Ap. J.* 661:236–49

Aharonian F, Akhperjanian AG, Bazer-Bachi AR, Beilicke M, Benbow W, et al. 2007e. *Astron. Astrophys.* 464:235–43

Aharonian F, Akhperjanian AG, Bazer-Bachi AR, Beilicke M, Benbow W, et al. 2008f. *Astropart. Phys.* 29:55–62

Aharonian F, Akhperjanian AG, de Almeida UB, Bazer-Bachi AR, Behera B, et al. 2008g. *Phys. Rev. D* 78:072008

Aharonian F, Buckley J, Kifune T, Sinnis G. 2008h. *Rep. Prog. Phys.* 71:096901

Aharonian F, Akhperjanian AG, de Almeida UB, Bazer-Bachi AR, Behera B, et al. 2009b. *Ap. J.* 692:1500–5

Aharonian FA. 1991. *Astrophys. Space Sci.* 180:305–20

Aharonian FA, Akhperjanian AG, Aye KM, Bazer-Bachi AR, Beilicke M, et al. 2004. *Nature* 432:75–77

Aharonian FA, Akhperjanian AG, Bazer-Bachi AR, Behera B, Beilicke M, et al. 2007f. *Astron. Astrophys.* 469:L1–4

Aharonian FA, Hofmann W, Rieger F, eds. 2008. *Proc. 4th Int. Meet. High Energy Gamma-Ray Astron., Heidelberg*, Vol. 1085. New York: AIP

Aharonian FA, Khangulyan D, Costamante L. 2008. *MNRAS* 387:1206–14

Albert J, Aliu E, Anderhub H, Antonelli LA, Antoranz P, et al. 2008a. *Ap. J.* 685:L23–26

Albert J, Aliu E, Anderhub H, Antonelli LA, Antoranz P, et al. 2008b. *Science* 320:1752–54

Albert J, Aliu E, Anderhub H, Antoranz P, Armada A, et al. 2006a. *Ap. J.* 648:L105–8

Albert J, Aliu E, Anderhub H, Antoranz P, Armada A, et al. 2006b. *Science* 312:1771–73

Albert J, Aliu E, Anderhub H, Antoranz P, Armada A, et al. 2007a. *Ap. J.* 664:L87–90

Albert J, Aliu E, Anderhub H, Antoranz P, Armada A, et al. 2007b. *Ap. J.* 658:245–48

Albert J, Aliu E, Anderhub H, Antoranz P, Armada A, et al. 2007c. *Ap. J.* 667:358–66

Albert J, Aliu E, Anderhub H, Antoranz P, Armada A, et al. 2007d. *Ap. J.* 665:L51–54

Albert J, Aliu E, Anderhub H, Antoranz P, Backes M, et al. 2008c. *Ap. J.* 684:1351–58

Albert J, Aliu E, Anderhub H, Antoranz P, Backes M, et al. 2008d. *Ap. J.* 679:428–31

Albert J, Aliu E, Anderhub H, Antoranz P, Backes M, et al. 2008e. *Phys. Lett.* B668:253–57

Aliu E, Anderhub H, Antonelli LA, Antoranz P, Backes M, et al. 2008. *Science* 322:1221–24

Amelino-Camelia G, Ellis J, Mavromatos NE, Nanopoulos DV, Sarkar S. 1998. *Nature* 393:763–65

Amenomori M, Ayabe S, Cao PY, Danzengluobu, Ding LK, et al. 1999. *Ap. J.* 525:L93–96

Asano K, Inoue S. 2007. *Ap. J.* 671:645–55

Aschenbach B. 1998. *Nature* 396:141–42

Atkins R, Benbow W, Berley D, Blaufuss E, Bussons J, et al. 2003. *Ap. J.* 595:803–11

Atoyan AM, Aharonian FA. 1996. *Astron. Astrophys. Suppl.* 120:C453–56

Benaglia P, Romero GE. 2003. *Astron. Astrophys.* 399:1121–34

Berezhko EG, Ksenofontov LT, Völk HJ. 2003. *Astron. Astrophys.* 412:L11–14

Berezhko EG, Völk HJ. 2006. *Astron. Astrophys.* 451:981–90

Bernlohr K. 2000. *Astropart. Phys.* 12:255–68

Bertone G, Zentner AR, Silk J. 2005. *Phys. Rev. D* 72:103517

Biller SD, Breslin AC, Buckley J, Catanese M, Carson M, et al. 1999. *Phys. Rev. Lett.* 83:2108–11

Blasi P, Gabici S, Brunetti G. 2007. *Int. J. Mod. Phys. A* 22:681–706

Blondin JM, Chevalier RA, Frierson DM. 2001. *Ap. J.* 563:806–15

Blumenthal GR, Gould RJ. 1970. *Rev. Modern Phys.* 42:237–71

Bringmann T, Bergström L, Edsjö J. 2008. *J. High Energy Phys.* 1:49

Buckley J, Baltz EA, Bertone G, Byrum K, Fegan S, et al. 2008a. Am. Phys. Soc. Comm. White Paper, Dark Matter Sci. Work. Group. *ArXiv* 0812.0795

Buckley J, Byrum K, Dingus B, Falcone A, Kaaret P, et al. 2008b. Am. Phys. Soc. Comm. White Paper, Dark Matter Sci. Work. Group. *ArXiv* 0810.0444

Caprioli D, Blasi P, Amato E, Vietri M. 2008. *Ap. J.* 679:L139–42

Carrigan S, Hinton JA, Hofmann W, Kosack K, Lohse T, et al. 2007. *Proc. 30th Int. Cosmic Ray Conf., Merida, Mexico*, 2007, Vol. 2:659–662 (ArXiv 0709.4094)

Casares J, Ribó M, Ribas I, Paredes JM, Martí J, Herrero A. 2005. *MNRAS* 364:899–908

Costamante L, Ghisellini G. 2002. *Astron. Astrophys.* 384:56–71

Daniel MK, Badran HM, Bond IH, Boyle PJ, Bradbury SM, et al. 2005. *Ap. J.* 621:181–87

de Jager OC, Djannati-Ataï A. 2008. In *Neutron Stars and Pulsars*, ed. W Becker, pp. 451–79. Astrophys. Space Sci. Lib., Vol. 357. New York: Springer

Dhawan V, Mioduszewski A, Rupen M. 2006. In *Microquasar Workshop: Microquasars and Beyond*, VIth, September 18–22, Como, Italy.

Domingo-Santamaría E, Torres DF. 2005. *Astron. Astrophys.* 444:403–15

Dondi L, Ghisellini G. 1995. *MNRAS* 273:583–95

Fan YZ, Wei DM, Xu D. 2007. *MNRAS* 376:1857–60

Ferrigno C, Blasi P, de Marco D. 2005. *Astropart. Phys.* 23:211–26

Fossati G, Buckley JH, Bond IH, Bradbury SM, Carter-Lewis DA, et al. 2008. *Ap. J.* 677:906–25

Franceschini A, Rodighiero G, Vaccari M. 2008. *Astron. Astrophys.* 487:837–52

Frieman JA, Turner MS, Huterer D. 2008. *Annu. Rev. Astron. Astrophys.* 46:385–432

Funk S, Hinton JA, Pühlhofer G, Aharonian FA, Hofmann W, et al. 2007. *Ap. J.* 662:517–24

Gabici S, Aharonian FA, Blasi P. 2007. *Astron. Astrophys. Suppl.* 309:365–71

Gaensler BM, Slane PO. 2006. *Annu. Rev. Astron. Astrophys.* 44:17–47

Gaitskell RJ. 2004. *Annu. Rev. Nucl. Part. Sci.* 54:315–59

Galaverni M, Sigl G. 2008. *Phys. Rev. D* 78:063003

Harding AK. 2007. *Acceleration and high energy emission from the polar cap and slot gap*. Invited talk at 363th Heraeus-Seminar on Neutron Stars and Pulsars, Bad Honnef, Germany, May 2006. *ArXiv e-prints* 0710.3517

Hartman RC, Bertsch DL, Bloom SD, Chen AW, Deines-Jones P, et al. 1999. *Astron. Astrophys. Suppl.* 123:79–202

Hauser MG, Dwek E. 2001. *Annu. Rev. Astron. Astrophys.* 39:249–307

Helfand DJ, Gotthelf EV, Halpern JP, Camilo F, Semler DR, et al. 2007. *Ap. J.* 665:1297–303

Hester JJ. 2008. *Annu. Rev. Astron. Astrophys.* 46:127–55

Hillas AM. 2005. *J. Phys. G Nucl. Phys.* 31:95–131

Hinton J. 2009. *New J. Phys.* In press. (*ArXiv* 803.1609)

Hinton JA, Aharonian FA. 2007. *Ap. J.* 657:302–7

Hinton JA, Skilton JL, Funk S, Brucker J, Aharonian FA, et al. 2009. *Ap. J.* 690:L101–4

Hofmann W. 2006. *Performance limits for Cherenkov instruments*. Talk presented at Cherenkov 2005 Workshop, Palaiseau. (astro-ph/0603076)

Hooper D, Baltz EA. 2008. *Annu. Rev. Nucl. Part. Sci.* 58:293–314

Hoppe S, for the H.E.S.S. Collaboration. 2007. *Proc. 30th Int. Cosmic Ray Conf., Mexico*, 2:579–82. *ArXiv* 0710.3528

Hunter SD, Bertsch DL, Catelli JR, Dame TM, Digel SW, et al. 1997. *Ap. J.* 481:205–40

Itoh C, Enomoto R, Yanagita S, Yoshida T, Asahara A, et al. 2007. *Astron. Astrophys.* 462:67–71

Itoh C, Enomoto R, Yanagita S, Yoshida T, Tanimori T, et al. 2003. *Astron. Astrophys.* 402:443–55

Johnston S, Manchester RN, Lyne AG, Bailes M, Kaspi VM, et al. 1992. *Ap. J.* 387:L37–41

Kardashev NS. 1962. *Sov. Astron.* 6:317–27

Katagiri H, Enomoto R, Ksenofontov LT, Mori M, Adachi Y, et al. 2005. *Ap. J.* 619:L163–66

Katarzyński K, Sol H, Kus A. 2001. *Astron. Astrophys.* 367:809–25

Kelner SR, Aharonian FA, Bugayov VV. 2006. *Phys. Rev. D* 74:034018

Kennel CF, Coroniti FV. 1984. *Ap. J.* 283:710–30

Khangulyan D, Aharonian F, Bosch-Ramon V. 2008. *MNRAS* 383:467–78

Kirk JG, Ball L, Skjaeraasen O. 1999. *Astropart. Phys.* 10:31–45

Krennrich F, Badran HM, Bond IH, Bradbury SM, Buckley JH, et al. 2001. *Ap. J.* 560:L45–48

Krennrich F, Bond IH, Bradbury SM, Buckley JH, Carter-Lewis DA, et al. 2002. *Ap. J.* 575:L9–13

Levinson A. 2000. *Phys. Rev. Lett.* 85:912–15

Leyder JC, Walter R, Rauw G. 2008. *Astron. Astrophys.* 477:L29–32

Lucek SG, Bell AR. 2000. *MNRAS* 314:65–74

Mannheim K. 1993. *Astron. Astrophys.* 269:67–76

Mattana F, Falanga M, Götz D, Terrier R, Esposito P, et al. 2009. *Ap. J.* 694:12–17

Mazin D, Raue M. 2007. *Astron. Astrophys.* 471:439–52

Meszaros P. 2006. *Rep. Prog. Phys.* 69:2259–322

Mirabel IF, Rodriguez LF. 1994. *Nature* 371:46–48

Moderski R, Sikora M, Coppi PS, Aharonian F. 2005. *MNRAS* 363:954–66

Moskalenko IV, Porter TA, Strong AW. 2006. *Ap. J.* 640:L155–58

Naumann-Godo M, Beilicke M, Hasuer D, Lemoine-Gourmard M, de Naurois M, et al. 2008. See Aharonian, Hofmann & Rieger 2008, pp. 304–7

Paredes JM, Martí J, Ribó M, Massi M. 2000. *Science* 288:2340–42

Pavlidou V, Fields BD. 2001. *Ap. J.* 558:63–71

Pe'er A, Waxman E. 2005. *Ap. J.* 633:1018–26

Perkins JS, Badran HM, Blaylock G, Bradbury SM, Cogan P, et al. 2006. *Ap. J.* 644:148–54

Persic M, Rephaeli Y, Arieli Y. 2008. *Astron. Astrophys.* 486:143–49

Pittard JM, Dougherty SM. 2006. *MNRAS* 372:801–26

Porter TA, Moskalenko IV, Strong AW. 2006. *Ap. J.* 648:L29–32

Primack JR, Gilmore RC, Somerville RS. 2008. See Aharonian, Hofmann & Rieger 2008, pp. 71–82

Protheroe RJ, Stanev T. 1993. *MNRAS* 264:191–200

Punch M, Akerlof CW, Cawley MF, Chantell M, Fegan DJ, et al. 1992. *Nature* 358:477–78

Rees MJ, Gunn JE. 1974. *MNRAS* 167:1–12

Reimer A, Pohl M, Reimer O. 2006. *Ap. J.* 644:1118–44

Reynolds SP. 2008. *Annu. Rev. Astron. Astrophys.* 46:89–126

Rieger FM, Mannheim K. 2002. *Astron. Astrophys.* 396:833–46

Stecker FW, Baring MG, Summerlin EJ. 2007. *Ap. J.* 667:L29–32

Stecker FW, de Jager OC, Salamon MH. 1992. *Ap. J.* 390:L49–52

Steigman G, Turner MS. 1985. *Nucl. Phys. B* 253:375–86

Strigari LE, Koushiappas SM, Bullock JS, Kaplinghat M, Simon JD, et al. 2008. *Ap. J.* 678:614–20

Strong AW, Moskalenko IV, Ptuskin VS. 2007. *Annu. Rev. Nucl. Part. Sci.* 57:285–327

Tavecchio F, Maraschi L, Ghisellini G. 1998. *Ap. J.* 509:608–19

Thompson DJ. 2004. *New Astron. Rev.* 48:543–49

Uchiyama Y, Aharonian FA, Tanaka T, Takahashi T, Maeda Y. 2007. *Nature* 449:576–78

Uchiyama Y, Takahashi T, Aharonian FA. 2002. *Publ. Astron. Soc. Jpn.* 54:L73–77

Vink J, Bleeker J, van der Heyden K, Bykov A, Bamba A, Yamazaki R. 2006. *Ap. J.* 648:L33–37

Vink J, Laming JM. 2003. *Ap. J.* 584:758–69

Völk HJ, Aharonian FA, Breitschwerdt D. 1996. *Space Sci. Rev.* 75:279–97

Wagner RM. 2008. *MNRAS* 385:119–35

Weekes TC, Cawley MF, Fegan DJ, Gibbs KG, Hillas AM, et al. 1989. *Ap. J.* 342:379–95

Wood M, Blaylock G, Bradbury SM, Buckley JH, Byrum KL, et al. 2008. *Ap. J.* 678:594–605

Zirakashvili VN, Aharonian F. 2007. *Astron. Astrophys.* 465:695–702

Zwicky F. 1939. *Proc. Natl. Acad. Sci. USA* 25:338–44